Development and assessment of the physical-biogeochemical ocean regional model in the Northwest Pacific: NPRT v1.0 (ROMS v3.9–TOPAZ v2.0)

Daehyuk Kim[1], Hyun-Chae Jung[4], Jae-Hong Moon[1,2,3], Na-Hyeon Lee[3]

[1] *Center for Sea Level Changes, Jeju National University, Jeju, 63243, Republic of Korea*

[2] *Department of Earth and Marine Sciences, Jeju National University, Jeju, 63243, Republic of Korea*

[3] *Faculty of Earth and Marine Convergence, Earth and Marine Science Major, Jeju National University, Jeju, 63243, Republic of Korea*

[4] *Department of Earth and Environmental Sciences, Jeonbuk National University, Jeonju, 54896, Republic of Korea*

Corresponding author: Jae-Hong Moon, jhmoon@jejunu.ac.kr

16   Abstract

17   The Northwest Pacific is characterized by the presence of the warm and nutrient-depleted Kuroshio

18   Current and the cold and nutrient-enriched Oyashio Current. In this region, surface primary production

19   leads to increased nutrient consumption and CO_2 exchange. The Yellow and East China Seas (YECS)

20   are predominantly influenced by freshwater input. A high resolution regional numerical model tailored

21   to the specific features of each area is required to reproduce the different characteristics of each region.

22   Therefore, to accurately analyze the physical and biogeochemical system, this study developed a new

23   coupled physical-biogeochemical model combining the three-dimensional Regional Ocean Modeling

24   System (ROMS) and the Generic Ocean Turbulence Model Tracers of Phytoplankton with Allometric

25   Zooplankton (TOPAZ) for the Northwest Pacific, including the YECS. The simulated physical and

26   biogeochemical variables in the ROMS–TOPAZ (NPRT) were evaluated by comparing them with

27   available observational data. NPRT successfully simulated the seasonal variability of chlorophyll and

28   nutrients, capturing two peaks in spring and autumn, which were not captured by the CMIP6 data.

29   Particularly in the YECS, NPRT effectively represented the high phytoplankton biomass driven by

30   riverine effect, which is difficult to reproduce in global biogeochemical model with low-resolution.

31   However, NPRT still exhibits significant biases in the subarctic region and marginal seas. To minimize

32   the uncertainties in biogeochemical variables, it is necessary to refine the initial and boundary

33   conditions, adjust parameters, and apply discharge forcing based on observational data. Despite these

34   limitations, NPRT is an important tool for studying the interaction between ocean physics and

35   biogeochemistry at a high resolution.

37   **1. Introduction**

38   The ocean biogeochemical processes are among the most important fields for understanding Earth's

39   carbon and ecosystem cycles, as well as the global climate system (Reid et al., 2009; Kang et al., 2017;

40   Park et al., 2014, 2018, Lee et al., 2022). Previous studies utilized Earth system models to analyze ocean

41   biogeochemistry, climate feedback, and the carbon cycle (Kang et al., 2017; Park et al., 2018; 2019). In

42   particular, significant efforts have been made to analyze physical–biogeochemical features at the global

43   scale as well as at regional scales (Hauri et al., 2020; Zhao et al., 2021; Wu et al., 2023; Na et al., 2024).

44   The North Pacific is a key region where the biological carbon pump occurs effectively (Chierici et

45   al., 2006; Takahashi et al., 2009). Low-frequency physical and ecological variabilities in the North

46   Pacific are closely related to various climatological variability patterns, such as the Pacific Decadal

47   Oscillation (PDO) and El Niño–Southern Oscillation (ENSO). Numerous studies have been conducted

on the responses of ecosystems to climatic and environmental conditions influenced by these long-term climatological variability patterns, especially in the Northeast Pacific (Overland et al., 2008; Yatsu et al., 2013; Ma et al., 2020). However, in the Northwest Pacific, including marginal seas, regional-scale oceanographic and ecological variabilities are independent across regions and show relatively weak linkages to climatological variability patterns, such as the PDO and ENSO (Jung et al., 2017; Ma et al., 2020). In particular, the Northwest Pacific is known as the Kuroshio–Oyashio Confluence Region (142–160° E, 35–40° N; Kawai, 1972; Hanawa and Mitsudera, 1987); the Oyashio Current is formed from the East Kamchatka Current, flowing southwestward along the Hokkaido coast while mixing with the Okhotsk Sea Mode Water, and the Kuroshio Current flows northeastward along the east of Japan, originating from Luzon Island (Nitani, 1972). Therefore, this region is known for the convergence of distinct water properties, resulting in a complex frontal structure, thermohaline mixing, and significant variability in the upper layer circulation (Qiu, 2001; Yasuda, 2003; Taguchi et al., 2007). Specifically, the water mass of the Oyashio Current has low temperature and low salinity, i.e., lower than 7 °C and 33.7 psu at a depth of 100 m (Kawai, 1972). Conversely, the water mass of the Kuroshio Current has a temperature higher than 14 °C and salinity higher than 34.7 psu (Nitani, 1972; Wang et al., 2022). In this region, the biogeochemical characteristics also exhibit significant regional differences. The cyclonic subarctic gyre, located west of the Oyashio Current, is characterized by high nutrient levels and low chlorophyll concentration (Taniguchi, 1999). Conversely, the anticyclonic tropical gyre, situated in the Kuroshio Current, is characterized by low nutrient levels (Siswanto et al., 2015). The interaction between gyres with distinct biogeochemical characteristics results in increased nutrient availability and the simulation of high phytoplankton biomass (Shiozaki et al., 2014). Consequently, the Northwest Pacific has been extensively studied from the perspectives of hydrography, climate change, nutrient transport, the carbon cycle, phytoplankton production, and community structure in relation to external conditions (Okamoto et al., 2010; Kuroda et al., 2019; Wang et al., 2021).

The Northwest Pacific is an important region for understanding the global carbon cycle and enhancing its predictability. Many previous studies have analyzed the carbon cycle, ecosystems, and future climate change using low-resolution global climate models with biogeochemical modules (Park et al., 2014; Jung et al., 2020; Hauri et al., 2020; Lee et al., 2022). However, coupled physical–biogeochemical ocean models with low horizontal resolutions involve limitations regarding accurately reproducing and analyzing the characteristics of oceanic environmental systems particularly the physical–biogeochemical factors in regional areas. Therefore, in this study, to accurately understand the physical–biogeochemical processes at the regional scale and address uncertainties, a regional ocean model and a biogeochemical model were coupled at a high resolution. Specifically, we employed the Generic Ocean Turbulence Model–Tracers of Phytoplankton with Allometric Zooplankton (TOPAZ)

82 developed by the US National Oceanic and Atmospheric Administration's Geophysical Fluid Dynamics
83 Laboratory (GFDL), in conjunction with the Regional Ocean Modeling System (ROMS).

84 This study introduces a new high-resolution coupled physical-biogeochemical model, named the
85 "Northwest Pacific ROMS–TOPAZ model version 1.0 (hereafter NPRT)", which is a valuable tool for
86 not only understanding the interactions between physical and biogeochemical processes but also for
87 predicting the future ocean carbon system. We describe and evaluate the simulation results of the
88 coupled physical–biogeochemical model (NPRT) through comparison with available observational data.
89 Sections 2.1 and 2.2 describe the characteristics of the models used in this study, and Section 2.3 and
90 2.4 elaborate on the developed NPRT, the methodology behind it, and the specific model design for the
91 study area. In section 3, the model results are evaluated using observations of physical and
92 biogeochemical variables, such as sea surface height (SSH), salinity, chlorophyll, nutrients, dissolved
93 inorganic carbon (DIC), Alkalinity (Alk) and dissolved oxygen (DO). In addition, we analyze the
94 characteristics of the physical–biogeochemistry regional ocean model with high resolution. Finally, a
95 summary is presented in section 4.

96

2. Data and model

97

2.1 Physical Ocean model (ROMS v3.9)

98

99 For conducting the physical–biogeochemical model coupling in this study, we employed ROMS
100 version 3.9 (hereafter ROMS; Song and Haidvogel, 1994), which is a popular physical regional ocean
101 model. ROMS is a three-dimensional primitive-equation physical ocean model that uses hydrostatic
102 and Boussinesq approximations. The horizontal grid system is the Arakawa-C grid system, which
103 enhances computational stability and efficiency (Arakawa and Lamb, 1977). The vertical coordinate
104 system is the S-coordinate (stretched terrain-following coordinate), which combines the advantages of
105 implementing the z-coordinate for the planetary boundary layer (PBL) and the σ-coordinate for the
106 bottom boundary layer. In this way, it allows for accurate analyses of physical phenomena in the
107 thermocline or bottom boundary layer, while reducing pressure gradient errors that are sensitive to the
108 terrain (Song and Wright, 1998; Shchepetkin and McWilliams, 2003).

109 ROMS can utilize horizontal advection schemes, such as second-, and fourth-order centered
110 differences and a third-order upstream scheme. Various options are available for vertical mixing,
111 including the K-profile parameterization (KPP; Large et al., 1994), M–Y (Mellor and Yamada, 1982),
112 Generic Length Scale (GLS; Umlauf and Burchard, 2003). In addition, bulk parameterization involving
113 the wind, sensible heat flux, and latent heat flux provides better calculations of the heat budget changes,

114 which is essential for elucidating the atmosphere–ocean interactions (Fairall et al., 1996). For more

115 information on ROMS, we refer to Shchepetkin and McWilliams (2005) and McWilliams (2009).

2.2 Biogeochemical model (TOPAZ v2.0)

117 TOPAZ version 2.0 (hereafter TOPAZ) is a biogeochemical module that simulates the cycles of

118 carbon, nitrogen, phosphorus, silicon, iron, DO, and lithogenic material, while also considering the

119 growth cycles of the zooplankton and phytoplankton. In biogeochemical processes, phytoplankton

120 members are categorized based on their sizes into small and large, including the nitrogen-fixing

121 diazotrophs. Overall, TOPAZ handles a total of 30 prognostic and 11 diagnostic tracers, and the state

122 variable C in various tracers reproduced in TOPAZ can be calculated using the following continuity

123 equation to describe local changes.

124 $$\frac{\partial C}{\partial t} = -\nabla \cdot \tilde{v}C + \nabla K \nabla C + S_c, \qquad (1)$$

125

126 where $\tilde{v}$ and K represent the vector velocity and diffusivity, respectively, and S_c indicates the source-

127 minus-sink terms of the state variable C calculated at each grid. TOPAZ considers eight types of

128 biogeochemical processes: the dissolved organic matter (DOM) cycle, particle sinking, dry/wet

129 atmospheric decomposition, gas exchange, river input, removal, sediment input and scavenging (Dunne

130 et al., 2005; 2007). Various equations for these processes are available, utilizing relationships between

131 variables derived from observational data (Dunne et al., 2012). In addition, TOPAZ includes an "optical

132 feedback" module that considers the chlorophyll photosynthesis. Optical feedback calculates the total

133 surface irradiance($I(z)$) as a function of the solar radiation wavelength (Manizza et al., 2005). This

134 scheme regulates vertically penetrating irradiance due to shortwave radiation absorption in the visible

135 light, which is influenced by the distribution of chlorophyll concentration in the water column of the

136 model.

137 $$I(z) = I_{IR} \cdot e^{-k_{IR}^2} + I_{RED(z-1)} \cdot e^{-k_{(r)}\Delta z} + I_{BLUE(z-1)} \cdot e^{-k_{(b)}\Delta z}, \qquad (2)$$

138

139 where the first term in the right hand side represents the penetration of the infrared wavelength band,

140 and the second and third terms represent the photosynthetically active radiation (PAR), which is divided

141 into two visible wavelength bands, namely the red and blue/green bands. PAR is used to calculate the

142 growth rate of phytoplankton groups and is a key factor in biogeochemistry. For more detailed

143 information on TOPAZ, we refer to Dunne et al. (2012).

144 In the TOPAZ model, there are not only the primary 11 diagnostic variables but also many secondary

145 diagnostic variables. Net primary production (NPP) was calculated using the secondary diagnostic

146 variables such as the maximum growth rate, temperature, nutrients, and light limitation factors
147 (Laufkötter et al. 2015). Unfortunately, the TOPAZ model used in this study does not store secondary
148 diagnostic variables related to NPP. Nevertheless, since it simulates various nutrients, chlorophyll
149 concentrations, and carbon cycles, the TOPAZ model can be effectively used to analyze biogeochemical
150 processes.

2.3 The coupled ROMS–TOPAZ model (NPRT version 1.0)

152 In this study, to couple ROMS with TOPAZ, we employed the stand-alone version of TOPAZ, which
153 was separated from the Modular Ocean Model version 5 (MOM5) developed by the GFDL in a previous
154 study (Jung et al., 2020). In this study for the stand-alone version of TOPAZ, the air–sea gas exchange
155 for CO_2 and O_2 is based on Wanninkhof (1992) and Najjar and Orr (1998), and the optical feedback is
156 based on Manniza et al. (2005). Furthermore, TOPAZ prescribes the surface flux from the atmosphere
157 to the ocean for nitrate (NO_3), ammonia (NH_4), lithogenic aluminosilicate (LITH), and dissolved iron
158 (Fed) (Jung et al., 2020). For these atmospheric chemistry values for the surface flux, this study employs
159 climatological monthly mean data as provided by the official MOM GitHub (https://mom-
160 ocean.github.io/docs/quick-start-guide/, last access: 1 March 2023).

161 Fig. 1 shows the structure of the NPRT. During the initialization process, TOPAZ receives the grid
162 and domain information from ROMS. Subsequently, integration with the *ROMS Main Driver* occurs to
163 calculate S_c within the "time step loop" using Eq. (1). Simultaneously, the chlorophyll optical feedback
164 is also considered in each time step, with the PAR modified by chlorophyll concentrations influencing
165 S_c, whereas the total radiation is used in the physical processes of ROMS. In the *ROMS Main Driver*,
166 the advection and diffusivity terms are calculated considering river runoff (Alk, DIC, NH_4, NO_3, LITH,
167 and PO_4). Information such as prognostic tracers, ocean physical variables, atmospheric forcing, and
168 dry/wet deposition (LITH, NH_4, NO_3, and Fed) are then transmitted to the TOPAZ module, where the
169 source/sink term (S_c) is calculated. In other words, the state variable *C* is calculated using data related
170 to the transport tendency of the tracers and source/sink term through the *ROMS physics* and
171 *generic_TOPAZ_column_physics* modules (Fig. 1).

2.4 Experimental setup

173 To operate NPRT, it is necessary to obtain the initial and boundary conditions for the
174 biogeochemical variables considered by TOPAZ; however, it is impossible to encompass all
175 biogeochemical observational data, since TOPAZ considers 30 prognostic and 11 diagnostic tracers.
176 Therefore, in this study, the results of MOM5–TOPAZ were employed as the initial and boundary
177 conditions of TOPAZ. To operate MOM5–TOPAZ, the default input datasets provided by the official

MOM GitHub were employed for the initial condition. MOM5–TOPAZ was initially operated for a 100-year spin-up integration under a pCO_2 environment (369.6 ppm) and ECMWF Reanalysis v5 (ERA5; Hersbach et al. 2020) of year 2000. Séférian et al. (2016) suggested that biochemical models require spin-up times longer than those required by physical ocean models. However, in this study, we adopted a 100-year spin-up time integration because of limited computing and time resources. After the 100-year spin-up time integration, using the results from the last time step as the initial condition, MOM5–TOPAZ was operated for 2000–2014, with a realistic atmospheric CO_2 concentration and atmospheric forcings from ERA5. Through these spin-up process described above, the initial and boundary conditions for the biogeochemical variables required to conduct NPRT were obtained. Nutrient concentrations for dry/wet atmospheric deposition and runoff were obtained from the default input data of the official MOM GitHub.

The initial and boundary conditions used for the physical variables were monthly mean data from the Hybrid Coordinate Ocean Model (HYCOM) reanalysis with a 1/12° (approximately 8 km) horizontal resolution. We used the six-hourly atmospheric external forcings, as provided by ERA5 as well as climatological monthly mean discharges of 12 major rivers, including the Yangtze, Huanghe, Yungsan, Keum, Han, Haihe, Luanhe, Amnokgang, Taedong, Qiantang, Pearl Rivers (Fig. 2; Kwon 2007). In addition, to obtain the tidal mixing effect, we considered 10 major tidal and tidal current harmonic components (M_2, S_2, N_2, K_2, K_1, O_1, P_1, Q_1, M_f, and M_m) from TPX07 (Egbert and Erofeeva, 2002). The GLS vertical mixing scheme was used for parameterization (Umlauf and Burchard, 2003). The bottom stress is parameterized with a quadratic drag law using a drag coefficient (2.5×10^{-3}), and horizontal viscosity and diffusion coefficients are 25 m^2 s^{-1} and 50 m^2 s^{-1}, respectively.

In this study, the model domain (105–170° E, 13–52° N) is the Northwest Pacific (NWP), which is one of the key regions for conducting global air–sea gas exchange, and includes the East/Japan Sea (hereafter East Sea), the Yellow and East China Seas (YECS), and South China Sea (Fig. 2). The horizontal resolution is 1/12°, both in longitude and latitude and the number of vertical layers is 50. The bottom topography from GEBCO data (Weatherall et al. 2015) is interpolated onto the model grid. NPRT was operated for a total of 15 years (2000–2014). To address the requirement for a sufficiently long spin-up time for executing the biogeochemical model, we conducted an additional spin-up for the initial five years. Therefore, in this study, the model results averaged over the last 10 years were used for the analysis.

To compare NPRT simulations with available observational data, in this study we divided the Northwest Pacific into four regions on the base of physical and biological environments: the NWP, further subdivided into subtropical (south of 40° N) and subarctic regions (north of 40° N), the East Sea,

211 and the YECS (Fig. 2). The SSH distribution was obtained from the Copernicus Marine Environment

212 Monitoring Service (CMEMS) satellite data from 2005–2014. Sea water temperature and salinity are

213 not only key factors in phytoplankton growth but also essential physical factors that determine the water

214 mass distribution in the ocean. In this study, the water temperature and salinity simulated from NPRT

215 were verified via annual and monthly climatological datasets from the World Ocean Atlas 2018

216 (WOA18) at a horizontal resolution of $1° \times 1°$. In addition, to evaluate the reproducibility of chlorophyll

217 concentrations, the Moderate Resolution Imaging Spectroradiometer (MODIS) and the Coupled Model

218 Intercomparison Project phase 6 (CMIP6; Eyring et al. 2016) were employed. As shown in Table 1, this

219 study adopted six models from CMIP6, providing chlorophyll concentrations for the historical period

220 (2005–2014). Each model is a single ensemble member, typically the 'r1i1p1f1' model: r, i, p, and f

221 denote the realization, initialization, physics, and forcing indices, respectively (Taylor et al. 2018). For

222 dissolved oxygen and nutrients, we also used annual and monthly climatological datasets from WOA18.

223 In addition, we utilized conductivity–temperature–depth (CTD) measurement data such as DO, from

224 the Japan Meteorological Agency (JMA) along the 137° E line from 2005–2014. The simulated DIC in

225 NPRT was compared with observational data from the Global Ocean Data Analysis Project version 2

226 (GLODAPv2; Lauvset et al., 2016) with a horizontal resolution of $1° \times 1°$ and 33 vertical layers from

227 0 to 5,500 m. GLODAPv2 is the mapped climatology field averaged from 1972–2013 at the Carbon

228 Dioxide Information Analysis Center (CDIAC).

229

3. Results and discussion

3.1. Physics

232   The study area is characterized by diverse oceanic environments, which determine the

233 biogeochemical characteristics. For example, in the Kuroshio–Oyashio Confluence Region, the

234 distributions of biogeochemical variables are determined by various physical and biological processes,

235 such as advection, horizontal mixing, vertical mixing, photosynthesis, and respiration. In addition, the

236 YECS is a river-dominated marginal sea, where large amounts of nutrients are discharged into the sea

237 along with freshwater (Dai et al., 2022; Na et al., 2024). Therefore, to accurately simulate the

238 biogeochemical properties, validating the oceanic physical characteristics, such as water temperature,

239 current, and salinity, is necessary. The distribution of ocean currents, in conjunction with water

240 temperature and salinity, is essential for determining the oceanic physical characteristics. This key factor

241 plays a fundamental role in direct and indirect assessments of all aspects of the marine environment. To

242 validate the reproducibility of the physical characteristics, the simulated SSH data were compared with

243   satellite-observed altimetry data from CMEMS.

244   Fig. 3 shows the long-term mean SSH distributions in CMEMS and NPRT during 2005–2014. The
245   Kuroshio Current originates from east of the Philippine coast, where it flows northeastward, passes
246   through the Tokara Strait, and continues eastward, meandering along the southern coast of Japan.
247   Furthermore, in the Shikoku Basin, there is a long-standing anticyclonic eddy associated with ocean-
248   bottom topography (Ding et al., 2022). In the subarctic region, the Oyashio Current flows southward
249   and converges with the Kuroshio Current, resulting in the mixing of distinct water masses; the region
250   where this happens is known as Kuroshio–Oyashio Confluence Region (Sugimoto and Hanawa, 2011;
251   Zhu et al., 2019). As mentioned previously, the NPRT results generally agree well with the observed
252   characteristics of the upper-layer circulation system in the NWP.

253   Fig. 4 shows the annual mean sea surface temperature (SST) in WOA18 and NPRT. The Northwest
254   Pacific exhibits subtropical characteristics, with high temperatures above 25 °C approximately 20° N.
255   Additionally, this region is predominantly influenced by the Kuroshio Current with warm water mass,
256   which results in the northward distribution of isotherms along the Japanese coast. As mentioned above,
257   a significant north–south temperature gradient is also observed between 35° N and 40° N, corresponding
258   to the Kuroshio–Oyashio Confluence Region. The characteristics of the SST distribution in the
259   Northwest Pacific are highly pronounced in NPRT, although the simulated sea surface temperature
260   predominantly shows a positive bias, with a particularly significant positive bias (> 4°C) observed in
261   the Kuroshio–Oyashio Confluence Region (Fig. 4c). Notably, the location of the Kuroshio–Oyashio
262   Confluence Region, which plays a crucial role in the formation of the North Pacific Intermediate Water
263   (NPIW), is also accurately simulated.

264   The NPIW is characterized by salinity and potential vorticity minima, with its primarily distributed
265   between density 26.6 and 27.2 σ_θ, corresponding to depths of 600–800 m (Lembke-Jene et al., 2017).
266   The NPIW transports large amounts of nutrients to the NWP. Therefore, simulating the NPIW is
267   important for the reproduction of biogeochemical characteristics in the NWP. Comparing the vertical
268   structures of zonal mean salinity between 140° and 160° E to those in the WOA18 data shows that the
269   depth of the salinity minimum layer is approximately 600–800 m, similar to the observational data (Fig.
270   5). However, the salinity minimum layer is about 0.2 psu higher than that of the observations. This is
271   attributed to a significant positive bias of salinity simulated in NPRT in Kuroshio–Oyashio Confluence
272   Region. Nevertheless, NPRT adequately reproduces not only the surface currents but also the ventilation
273   for the formation of the NPIW.

274   The YECS are characterized by the dominant effects of tidal mixing and runoff. Freshwater
275   discharged from the Yangtze River, one of the major sources of nutrients in the East China Sea, forms

a low-salinity plume that spreads and influences the stratifications of the surrounding areas (Moon et al., 2009). NPRT did not include all rivers in the YECS; nevertheless, a total of 12 rivers, including the Yangtze River, were included (Fig. 2). Regarding the oceanographic characteristics of the YECS, the model exhibits similar patterns with those of the observations from WOA18, despite of a negative bias (Fig. 6 and Supplement Fig. 1). During winter (February; Fig. 6e and Supplement Fig. 1e), the simulated sea surface salinity distribution in the YECS is below 32.0 psu, whereas during the freshwater discharge-intensive summer (August; Fig. 6f and Supplement Fig. 1f), the salinity drops below 30 psu, forming a low-salinity tongue shaped feature extending toward the Korean coast. In the NWP, high salinity water (> 34.0 psu) extends northward to around 40° N during winter and around 35° N during summer. The reproduced distinct seasonal variability is similar to that in the WOA18 data, with all spatial correlation coefficients and root-mean-square error (RMSE) for surface salinity distribution in the annual mean, winter, and summer being over 0.93 and 0.33–0.42 psu, respectively.

Overall, NPRT reasonably simulates the major characteristics observed in each region and is, therefore, suitable for analyzing the spatiotemporal distribution and characteristics of chlorophyll concentration, nutrients, and the carbon cycle influenced by these physical properties.

3.2. Biogeochemistry

3.2.1 Nutrients

The results of the simulated nitrates, phosphates, and silicates, which are essential for the growth of phytoplankton, were compared with the results of the observationally base WOA18 climatology (Figs. 7–9). Fig. 7a–c shows the comparison of the simulated surface annual mean nitrates with the observed ones. The distribution of the annual mean surface nitrate concentration in the observational data reveals a characteristic increase from low to high latitudes, with concentrations exceeding 15 µmol kg^{-1} in the subarctic region (Fig. 7a). In the model results, the annual mean concentration of nitrate also increases with increasing latitude and is predominantly distributed in the East Sea, Okhotsk Sea, and the Oyashio extension region (Fig. 7b). Compared with that in the observations, the overall distribution of annual mean surface nitrate concentrations is underestimated (Fig. 7c). In particular, in the subarctic region, the model results exhibit a large negative bias of over -10 µmol kg^{-1}, whereas in the East Sea and the Kuroshio and its extension regions, it exhibits a positive bias. The pattern correlation and RMSE for nitrate in the study area are 0.83 and 5.70 µmol kg^{-1}, respectively. The distribution of the annual mean surface phosphates in NPRT is similar to that in WOA18 (pattern correlation: 0.83; Fig. 8a, b). However, there is a negative bias in the subarctic region and a positive bias in the eastern coast of Sakhalin and

308   the East Sea (Fig. 8c). The bias range is approximately -1.2–0.5, and the RMSE is approximately 0.53

309   µmol kg^{-1}. Unlike other nutrients, the simulated silicate exhibits a significant positive bias (> 30 µmol

310   kg^{-1}) and a negative bias (> 30 µmol kg^{-1}) in the YECS and the subarctic region, respectively (Fig. 9c).

311   The vertical errors of the zonally averaged annual mean nutrients (nitrate, phosphate, and silicate) in

312   the NWP were overestimated south of the Kuroshio–Oyashio Confluence Region (40° N) until a depth

313   of 500 m (Fig. 10). However, in the 500–1500 m, the underestimation error in the 500–1500 m appears,

314   which seems to be related to the NPIW simulation. In the intermediate layer of the NWP, the subarctic

315   intermediate water nutrient pool (SINP) with high nutrient concentrations appears along with the NPIW

316   formed in the Kuroshio–Oyashio Confluence Region (Nishioka et al., 2020; 2021). However, it is

317   considered that the SINP is not distinct in NPRT due to the negative bias in the subarctic region, which

318   is the source of the SINP. Positive biases for nutrients were distributed within a depth of 500 m in all

319   seasons, similar to the annual mean bias, whereas negative biases exhibited in deeper depths (black

320   solid line in Fig. 10c, f, i). Regardless of the season, the depth of the positive bias peak for all nutrients

321   is approximately 100–300 m.

322   The simulated surface nutrient concentrations in NPRT exhibited a clear seasonal variability (Figs.

323   7–9). In winter, high nitrate concentrations distributed in the subsurface are supplied to the surface by

324   vertical mixing, resulting in an increase in the upper–layer nutrient concentrations from winter to spring.

325   In summer and autumn, distinct seasonal variability is observed, with concentrations gradually

326   decreasing owing to enhanced stratification. The temporal correlation coefficients between the model

327   results and observations (WOA18) for nutrients (nitrate, phosphate, and silicate) are approximately

328   0.78–0.98, indicating that the seasonal variability is well represented, except for the silicate

329   concentration in the YECS (temporal correlation coefficient: 0.47). In the subarctic region, all nutrients

330   are consistently underestimated regardless of the season, which is likely attributed to the initial and

331   boundary biogeochemical conditions. The initial conditions for nutrients derived from the MOM5–

332   TOPAZ results are approximately 10 µmol kg^{-1} lower than those derived from the WOA18 data (not

333   shown here).

334   In addition, we need to give particular attention to the overestimation of silicate in the YECS (Fig.

335   9). In TOPAZ, silicate is regulated through biogeochemical processes such as dissolution and uptake by

336   large phytoplankton within the mixed layer, as well as by particles sinking into the deep ocean (Dunne

337   et al. 2012). In NPRT, the overestimation of the silicate concentration can be attributed to two possible

338   factors. The first possibility is that silicate, unlike other nutrients, is only considered taken up by large

339   phytoplankton. The second factor is that the YECS, which is a shallow marginal sea with a maximum

340   depth of less than 50 m, experiences strong vertical mixing throughout the entire water column due to

strong winds, surface heat fluxes during winter, and tidal effects. In shallow marginal seas, rather than a decrease in the upper layer silicate concentration due to particles sinking into the deep ocean, it is speculated that particles remain within the mixed layer, continuously increasing through dissolution. To address the large bias in silicates observed in marginal seas such as the YECS, it is necessary to consider the specific marine environment of each region and adopt accurate parameters and external forcings.

To statistically evaluate the reproducibility of NPRT, this study calculated the monthly Taylor diagram score (TD score; Taylor, 2001; Jin et al. 2023) in each region (Table 1) via the following formulation.

$$TD \ (Taylor \ diagram) \ Score = \ |1 - R| + \left|1 - \frac{\sigma_M}{\sigma_O}\right| + \frac{E'}{\sigma_O} \ , \qquad (3)$$

where R is the pattern correlation, and where σ_M and σ_O indicate the standard deviations in the model and observations, respectively. E' is the RMSE. The TD scores for nitrate and phosphate concentrations tend to increase from summer to winter, except in the Subarctic region. In particular, the TD scores for nitrate in the subtropical region sharply increase in November and December (Table 1), which is due to the large bias distribution in the Kuroshio–Oyashio Confluence Region (not shown here). The positive bias distributed in this region is thought to be due to the relatively high nutrient concentrations in the subsurface in NPRT, which are transported to the surface layer through vertical mixing (Fig. 10). In the Subarctic region, the TD scores for all nutrients are greater than 2.5 (Table 1), but as mentioned above, the seasonal variability is well reproduced. Therefore, the dominant negative bias is expected to improve significantly with the use of more accurate initial and boundary conditions. The TD scores for nitrate and phosphate in the East Sea and the YECS are approximately 1.0–2.5 higher than those in the subtropical region. In the case of silicate, the TD score was greater than 10.0 for all months.

3.2.2 N:P ratio

The study area, the Northwestern Pacific, can be broadly divided into three limitation regions: the subtropical and subarctic regions and the YECS, which are characterized by nitrogen limitation (Browing et al. 2022), Fe limitation (Watson, 2001; Zhang et al 2021), and phosphate limitation (Lee et al. 2023), respectively. The N:P molar ratio in seawater is commonly used to evaluate whether the growth of phytoplankton is potentially limited by nitrogen or phosphorus. Fig. 11 shows the distribution pattern of the N:P molar ratio in the Northwestern Pacific. In the subtropical region, the N:P molar ratios in WOA18 and NPRT were approximately 3.4 and 4.3, respectively. However, NPRT shows a clear positive bias in the Kuroshio Current and its extension region. This characteristic is also evident in the

373   distribution of nutrient biases (Fig. 11c). The large meander of the Kuroshio Western Boundary Current

374   significantly influences not only physical characteristics but also biological processes (Hayashida et al.

375   2023). Therefore, to analyze the biological processes in the Kuroshio meandering region in accurately

376   the future, improving the model's representation of Kuroshio meandering is important. In WOA18, the

377   N:P molar ratio in the YECS was approximately 7.3, with the ratio exceeding 16.0, particularly in the

378   Yangtze River estuary, where a distinct phosphate limitation region was observed (Fig. 11a). However,

379   the simulated N:P ratio was relatively lower than the observed values in the Yangtze River estuary (Fig.

380   11b). As mentioned earlier, despite the significant influence of river discharge in regions such as the

381   YECS, the relatively low N:P molar ratio simulated in this study is likely due to inaccuracies in the

382   estimated nutrient input from riverine sources.

383

3.2.3 Chlorophyll

385   The characteristics of the simulated chlorophyll distributions were compared with those inferred

386   from the MODIS satellite data (Fig. 12). The chlorophyll concentrations derived from satellite data

387   include both sea surface and mixed layer components because of the backscattering effect of reflected

388   light (Park et al., 2014; Jochum et al., 2019; Jung et al., 2020). Therefore, in this study, 0–20 m depth-

389   averaged chlorophyll concentrations from NPRT were compared with satellite data from 2005–2014.

390   Although NPRT was conducted with external forcings that include interannual variations, the results

391   may have several uncertainties due to insufficient spin-up time and/or climatological data for river input

392   and atmospheric deposition. In addition, we analyzed the characteristics of the high-resolution regional

393   model (NPRT) compared with the global biogeochemical models in the CMIP6 datasets.

394   Biogeochemical models include various variables, among which the chlorophyll concentration is

395   influenced by physical factors (temperature and circulation system), light, and various nutrients, and it

396   exhibits distinct seasonal variability. In this study, we considered it a representative variable for

397   evaluating the performance of biogeochemical models and used a total of 13 ensemble members in the

398   CMIP6 models (Table 2). Among the 13 members (Table 2), ensemble numbers 1 to 8 were calculated

399   using the 0–20 m depth averaged chlorophyll concentration, whereas the remaining ensembles provided

400   only surface data. In addition, we compared the chlorophyll concentrations of GFDL–ESM2M and

401   GFDL–ESM2G (hereafter ESM2M and ESM2G), which are published in the Fifth Assessment Report

402   of Intergovernmental Panel on Climate Change (IPCC AR5), with the NPRT results. Since the historical

403   data for ESM2M and ESM2G are available only up to 2005, we analyzed the data from 1996 to 2005.

404   Since the chlorophyll distribution and seasonal variation exhibit different characteristics in each

405   region, the analysis in this study was divided into subtropical and subarctic regions, the East Sea, and

406   the YECS. First, when the data from subtropical and subarctic regions and the East Sea are analyzed,

407   the chlorophyll concentrations generally increase from low to high latitudes according to observations

408   (Fig. 12a). In NPRT, the distribution of the annual mean chlorophyll concentration was similar to the

409   observations in the subtropical region and East Sea (pattern correlations: 0.72 and 0.61, respectively).

410   However, a positive bias is dominant regardless of season, primarily due to the positive bias in nutrients

411   related to phytoplankton growth (Figs. 7–9). Despite the positive biases in the chlorophyll concentration

412   distributions in the subtropical and subarctic regions and the East Sea, as represented in NPRT, the

413   seasonal variation in the chlorophyll concentration, which has spring and autumn biomass peaks, was

414   similar to the observations (Fig. 13a, b, c). The reproducibility of seasonal variability in NPRT is

415   comparable to the results of ESM2M and ESM2G. However, most of the results of the CMIP6 models

416   do not adequately capture the autumn peak in the subtropical and subarctic regions and East Sea. The

417   pattern correlation ranges of the annual mean chlorophyll concentrations for each ensemble member of

418   CMIP6 in the subtropical and subarctic regions and the East Sea are -0.06–0.61, -0.39–0.65 and -0.15–

419   0.17, respectively (Fig. 14). Some models in the CMIP6 datasets show negative pattern correlations.

420   Although ESM2M and ESM2G were well represented, the range of pattern correlation coefficients was

421   quite low, ranging from -0.12–0.26. As a result, the TD scores in NPRT are lower than those in the

422   ESM2M, ESM2G, and CMIP6, especially in the East Sea, and the reproducibility of the chlorophyll

423   concentration distribution has significantly improved (Table 3).

424   In the YECS, the spatial correlation coefficient in NPRT was approximately 0.45 (Fig. 12a, b and

425   14d), which was relatively low compared with that in the other regions. However, the NPRT-simulated

426   biomass blooms near the Yangtze River and along the Chinese coast were driven by high freshwater

427   discharge (Fig. 12b). In addition, NPRT, ESM2M and ESM2G effectively reproduced the seasonal

428   variability (spring peak and increasing from summer) that was not captured by the CMIP6 models. In

429   the case of the CMIP6 models, negative bias is dominant regardless of the season (Fig. 13d), and they

430   also lack clear seasonal variability in the chlorophyll concentration. In the YECS, the discharge of

431   freshwater and nutrient concentrations from rivers is one of the most important input forcings

432   determining the spatiotemporal pattern and variability (Zhou et al., 2008). In this study, to apply

433   observation data for freshwater discharge and nutrient concentrations from river outflows, tracer

434   concentrations were determined with a volume flux at the river source point, following an approach

435   similar to that adopted in regional biogeochemical models such as FENNEL (Fennel et al. 2006) and a

436   modified version of the Carbon, Ocean, Biogeochemistry and Lower Trophic (COBALT; Hauri et al.

437   2020). However, the chlorophyll concentrations in NPRT still tend to be underestimated (RMSE: 1.62

438   μmol kg^{-1}) in the YECS, including the Yangtze River estuary (Fig. 12c). Nonetheless, the TD score in

439   NPRT was approximately 2.32, which is lower than that in ESM2M, ESM2G, and CMIP6 (2.23–3.5)

440 (Table 3), and NPRT reproduced the seasonal variability (Fig. 13d) and spatial characteristics such as

441 biomass blooms near the Yangtze River and along the Chinese coast, driven by high freshwater

442 discharge (Fig. 12b).

443   In the YECS, the underestimated chlorophyll concentration in NPRT may also be related to the

444 distribution of low nutrient concentrations in the YECS. Furthermore, this can be attributed to the

445 incomplete consideration of the influences exerted by numerous rivers along the Chinese and Korean

446 coasts as well as the utilization of default data provided by MOM GitHub, which deviates from the

447 actual diverse biogeochemical variables (LITH, NH_4, NO_3, and Fed) introduced from the atmosphere.

448 In addition, we need to consider the uncertainties associated with the satellite observational data from

449 MODIS. MODIS indirectly estimates chlorophyll concentrations by measuring the spectrum of light

450 reflected from the sea surface (visible and near-infrared); however, completely eliminating the influence

451 of colored dissolved organic matter (CDOM) and suspended particles in the water is difficult. Coastal

452 regions, classified as type II waters, are particularly prone to bias in estimated surface chlorophyll

453 concentrations because of the high concentrations of CDOM and suspended particles (Mauri et al.

454 2007). The CDOM calculated using MODIS data was significantly greater in the YECS than in the

455 other regions (Supplement Fig. 2), and the absorption of blue light by CDOM can lead to an

456 overestimation of the chlorophyll concentration (Fig. 12 and Supplement Fig. 2). In other words, owing

457 to the influence of CDOM, the chlorophyll distribution observed by MODIS may be overestimated,

458 potentially leading to a negative bias in the chlorophyll simulated by NPRT in the YECS. Furthermore,

459 CDOM enhances shortwave heating at the surface while reducing it below the surface (Kim et al.

460 2016). This process can influence penetrating shortwave radiation, mixing, and surface heat flux.

461 Focusing on the variability in physical processes caused by CDOM could greatly contribute to

462 future research on the interactions between biogeochemistry and physical oceanography.

463

464   **3.2.4 Dissolved inorganic carbon and alkalinity**

465   The variables of the carbon system, including dissolved inorganic carbonic (DIC) and alkalinity

466 (Alk), simulated in NPRT were analyzed. First, DIC is a crucial component of ocean biogeochemistry

467 and is directly linked to plankton photosynthesis and respiration; hence, it is a valuable parameter for

468 the analysis of the carbon system (Ding et al., 2018). The results of NPRT, averaged from 2005–2014,

469 were compared with the observed climatological data obtained from GLODAPv2 (Fig. 15a–c). For both

470 the model results and observational data, the annual mean surface DIC concentration in the subarctic

471 region is significantly higher than that in the subtropical region. The simulated annual mean surface

472 DIC concentration in NPRT generally exhibited a positive bias. However, in the YECS, there was a

473 significant negative bias of over -300 µmol kg^{-1}. In particular, low DIC concentrations (below 1,900

474 µmol kg^{-1}) appeared in the Yangtze River estuary. The bias range for the entire study area is

475 approximately between -650 and 180 µmol kg^{-1}, with a pattern correlation of approximately 0.41 and a

476 RMSE of 99.84 µmol kg^{-1}. The GLODAPv2 dataset does not seem to adequately reproduce the low

477 DIC concentrations caused by discharge from the Yangtze River. This is because previous studies using

478 ship-based observations reported that low concentrations are distinctly observed in the Yangtze River

479 estuary (Zhai et al., 2007; Wang et al., 2016). If the YECS are not considered, the pattern correlation

480 and RMSE excluding the YECS are approximately 0.81 and 95.67 µmol kg^{-1}, respectively.

481   The Alk simulated in NPRT also exhibited a significant positive bias (> 150 µeq kg^{-1}) in the study

482 area, excluding the YECS (Fig. 15d–f). The overestimation of Alk in NPRT facilitates the accumulation

483 of pCO$_2$ from the atmosphere into the ocean, which may contribute to the increase in the surface DIC

484 concentration. The simulated annual mean surface CO$_2$ flux was predominantly characterized by an

485 influx from the atmosphere to the ocean (Fig. 16). However, it may be premature to conclude that the

486 results of carbonate variables in NPRT are positively biased because the time series of DIC

487 concentrations in MOM5–TOPAZ did not reach the equilibrium state during the spin-up period

488 (Supplement Fig. 3). Consequently, the initial and boundary conditions derived from the MOM5–

489 TOPAZ model results exhibit significantly higher DIC concentrations and Alk values than the

490 observations do. In particular, the DIC concentration at the eastern boundary is higher than that

491 observed, which may contribute to the elevated DIC levels in the subtropical region due to the influence

492 of the North Equatorial Current and Kuroshio Current. To improve this bias, more accurate boundary

493 conditions must be considered.

494

495   **3.2.5 Dissolved Oxygen**

496   DO is important for analyzing the ecological and physical characteristics of marine

497 ecosystems and serves as a tracer. It is associated with ocean temperature, air–sea exchange,

498 and phytoplankton photosynthesis. The simulated DO results were compared with the WOA18

499 climatological data and observations from the JMA (Figs. 17 and 18). Both the observations (i.e.,

500 WOA18) and the model results demonstrate a typical increase in surface DO concentrations from low

501 to high latitudes, with high concentrations of DO more than 300 µmol kg^{-1} being distributed in the

502 Okhotsk Sea and the Oyashio region (Fig. 17). With respect to that of the WOA18 observations, the

503 model tends to underestimate DO exhibiting a dominant negative bias (up to approximately -30 µmol

504 kg^{-1}) in the Oyashio region. The pattern correlation and the RMSE of DO concentration between the

505 model results and WOA18 data are 0.99 and 9.99 µmol kg^{-1}, respectively. The primary cause of the

negative bias in the simulated DO is related to the positive bias in surface temperature (Fig. 4c and 17c), which is thought to be due to the weakening of thermal solubility. To compare the vertical structures of DO, ship measured DO data from the JMA were employed along the 137° E line across the Kuroshio main path in January and June (Fig. 18). Both the observations and the model results show the presence of an oxycline layer, where the DO decreases sharply with depth. Below this layer, DO minimum zone is evident. However, the depth of the DO minimum zone in NPRT appears below 500 m regardless of the season, similar to the observations (JMA); however, the minimum DO concentrations are approximately 25 µmol kg^{-1} higher than the JMA data. This is presumed to be caused by the weak NPIW formation. These characteristics are also evident in the results obtained using the TOPAZ module (Lee et al., 2022). Consequently, NPRT adequately qualitatively reproduces the spatiotemporal distribution of the DO circulation system. However, sufficient observational data, accurate initial and boundary conditions, improvement in physical processes simulation, and adequate spin-up times are required for quantitative and reproducibility improvements, particularly in the intermediate layer.

4. Conclusions

The coupled physical–biogeochemical ocean model developed in this study, namely ROMS–TOPAZ (NPRT v1.0), is a preliminary investigation that reflects the characteristics of local regions with high resolution, enabling analysis of the interactions between the physical and biogeochemical processes in the ocean. The study area comprises the NWP, East Sea and YECS, which exhibit diverse characteristics depending on the region. The study area is one of the main regions where nutrients are consumed by primary production. CO_2 exchange between the air and sea is dominant in the NWP (Takahashi et al., 2009; Ishizu et al., 2021); however, in the YECS, the biogeochemical environment is significantly influenced by riverine discharge (Zhou et al., 2008). In these oceanic regions with such diverse features, we evaluated the reproducibility of the spatial distribution and seasonal variability of the physical and biogeochemical variables derived using NPRT. To generate the initial and boundary data for the biogeochemical variables required to simulate NPRT, first, MOM5–TOPAZ was integrated for 100 years under the pCO_2 environment, and ERA5 was integrated for 2000, after which it was conducted for an additional 15 years under actual atmospheric CO_2 concentration conditions (2000–2014). Using the biogeochemical variables reproduced by MOM5–TOPAZ and the physical variables from HYCOM, NPRT was subsequently integrated for 15 years (2000–2014). In this study, model results from the last 10 years (2005–2014) were used in the analysis.

NPRT successfully reproduced the overall spatial distributions, such as upper-layer circulation, the NPIW formation via ventilation, and salinity in the YECS influenced by freshwater input, as well as the

seasonal variability in biogeochemical variables. For nutrients (nitrate, phosphates, and silicate), there was a high pattern correlation coefficient for the annual mean surface nutrient concentrations. In particular, both pattern correlation coefficients for nitrate and phosphate concentrations in the study area are approximately 0.83, but the coefficient for silicate is low (approximately 0.42). All nutrients were underestimated in the subarctic region regardless of season, likely because low values were prescribed for the initial and boundary conditions. In contrast, the Kuroshio–Oyashio Confluence Region, characterized by strong vertical mixing, exhibited a positive bias, especially during winter, due to the relatively high nutrient concentrations at the subsurface in NPRT. Although biases are distributed depending on the region, the overall seasonal variability in all nutrients is well simulated. The temporal correlation coefficients for nutrients are approximately 0.78–0.98 in the study area, except for the silicate content in the YECS. In marginal seas at shallow depths, such as the YECS, silicate is presumed to accumulate continuously because of insufficient reduction caused by phytoplankton uptake and particles sinking into the deep ocean due to strong vertical mixing, leading to a significant positive bias. In other words, parameter adjustments considering physical and biogeochemical environments are necessary.

For chlorophyll concentration, although NPRT showed positive and negative biases in the study area, it effectively reproduced not only the seasonal variation in the subtropical and subarctic regions, East Sea, and YCES, but also the improved TD scores in all regions compared with the ESM2M, ESM2G, and CMIP6 data. In addition, in the YECS, because a significant amount of nutrients is discharged from the Yangtze River along with a large amount of freshwater, leading to biomass blooms around the Yangtze River estuary, the chlorophyll concentrations start to increase in July. As a result, low DIC concentrations associated with river effects were also simulated around the Yangtze River. These regional characteristics are difficult to reproduce via low-resolution global models. Furthermore, in the subtropical and subarctic regions, significant positive biases for DIC and Alk were predominantly simulated, which is due to the spin-up time (100 years) in this study being insufficient for reaching the equilibrium state.

In summary, the coupled model NPRT developed in this study is an important tool for studying the interactions between ocean physics and biogeochemistry at a high resolution, enabling research at the regional scale. In the future, this tool is expected to provide a basis for understanding the mechanisms of oceanic physics and biogeochemical environments in various regions, ultimately improving the accurate assessment and predictability of carbon cycling.

Acknowledgments.

This work has been supported by Basic Science Research Program through the National Research Foundation of Korea (NRF) funded by the Ministry of Education (RS-2024-00451970 and RS-2024-00461585), and the National Research Foundation of Korea (NRF) grant funded by the Korea government (MIST) (NRF-2022M3I6A1086449). The main calculations were performed by using the supercomputing resource of the Korea Meteorological Administration (National Center for Meteorological Supercomputer).

Code Availability.

ROMS–TOPAZ (NPRT v1.0) used in this study is archived on Zenodo (https://doi.org/10.5281/zenodo.11218350). In addition, the input data (initial, boundary, atmospheric forcings, atmospheric deposition data) for conducting NPRT and the model results are archived on Zenodo (https://zenodo.org/records/13941078). In addition, the plot scripts are uploaded (https://zenodo.org/records/15228135).

Data availability statement.

The data analyzed in this study are available from public websites. Bathymetric data were provided by GEBCO (GEBCO Compilation Group, 2021; GEBCO_2021 Grid, https://doi.org/10.5285/c6612cbe-50b3-0cffe053-6c86abc09f8f, GEBCO, 2022, last access: 1 March 2023). The atmospheric forcings were provided by ECMWF Reanalysis v5 (ERA5; https://cds.climate.copernicus.eu/cdsapp#!/search?type=dataset:1 March 2023). For conducting the MOM–TOPAZ model, the input data for initial, boundary, and dry/wet atmospheric deposition were provided by MOM GitHub (https://mom-ocean.github.io/docs/quick-start-guide/, last access: 1 March 2023). For conducting NPRT, the physical ocean initial and boundary data were used from Hybrid Coordinate Ocean Model (HYCOM; https://tds.hycom.org/thredds/catalog.html:1 December 2023). The SSH data were obtained from the Copernicus Marine and Environment Monitoring Service (CMEMS; http://marine.copernicus.eu, last access: 15 November 2023). The data used to evaluate the model results in this study are freely available online from Japan Meteorological Agency (JMA; https://www.data.jma.go.jp/gmd/kaiyou/db/vessel_obs/data-report/html/ship/ship_e.php), World Ocean Atlas 2018 (WOA18; https://www.ncei.noaa.gov/access/world-ocean-atlas-2018), , Moderate Resolution Imaging Spectroradiometer (MODIS; http://www.daac.gsfc.nasa.gov/data/dataset/ MODIS/) for chlorophyll concentration, and GLODAPv2 (GLODPAv2; (https://www.ncei.noaa.gov/access/ocean-carbon-acidification-data-system/

605 oceans/GLODAPv2_2022) for dissolved inorganic carbon. The CMIP6 model datasets are freely

606 available online (https://aims2.llnl.gov/search/cmip6, last access: 1 December 2023). Discharge data

607 for Yangtze River dataset are available online (https://www.cjh.com.cn/, last access: 24 September

608 2023). Unfortunately, discharge data for other rivers cannot be made publicly available. The colored

609 dissolved organic matter (CDOM) is freely available online (https://oceandata.sci.gsfc.nasa.gov/l3/,

610 last access: 15 January 2025).

611

612 *Author Contribution.*

613   DK, HCJ, and JHM designed the study. DK and HCJ conducted the models and the simulations

614 and primarily responsible for developing ROMS–TOPAZ (NPRT v1.0). NHL analyzed CMIP6 data.

615 All authors analyzed and discussed the results and contributed to writing and editing of the article.

616

617 *Competing interests.*

618   The authors declare that they have no conflict of interest.

619

620

621

622

623

624

625

626

627

628

629

630

631

632

633

634

635

636

References

Arakawa, A. and Lamb, V. R.: Computational design of the basic dynamical processes of the UCLA general circulation model, in: General circulation models of the atmosphere, Meth. Comput. Phys., edited by: Chang, J., Elsevier, 17, 173–265, https://doi.org/10.1016/B978-0-12-460817-7.50009-4, 1977.

Browning, T. J., Liu, X., Zhang, R., Wen, Z., Liu, J., Zhou, Y., Xu, F., Cai, Y., Zhou, K., Cao, Z., Zhu, Y., Achterberg, E. P., and Dai, M.: Nutrient co-limitation in the subtropical Northwest Pacific, Limnol. Oceanogr. Lett., 7, 52–61, https://doi.org/10.1002/lol2.10205, 2022.

Chierici, M., Fransson, A., and Nojiri, Y.: Biogeochemical processes as drivers of surface fCO$_2$ in contrasting provinces in the subarctic North Pacific Ocean, Global Biogeochem. Cycles, 20, GB1009, https://doi.org/10.1029/2004GB002356, 2006.

Dai, M., Su, J., Zhao, Y., Hofmann, F. E., Cao, Z., Cai, W.-J., Gan, J., Lacroix, F., Laruelle, G. G., Meng, F., Müller, D., Regnier, P. A.G., Wang, G., and Wang, Z.: Carbon fluxes in the coastal ocean: synthesis, boundaty processes, and future trends, Annu. Rev. Earth Planet. Sci., 50, 593-626, https://doi.org/10.1146/annurev-earth-032320-090746, 2022.

Ding, L., Ge, T., Gao, H., Luo, C., Xue, Y., Druffel, E.R.M., and Wang, X.: Large variability of dissolved inorganic radiocarbon in the Kuroshio extension of the Northwest North Pacific, Radiocarbon, 60, 691–704, https://doi.org/10.1017/RDC.2017.143, 2018.

Ding, Y., Yu, F., Ren, Q., Nan, F., Wang, R., Liu, Y., and Tang, Y.: The physical-biogeochemical responses to a subsurface Anticyclonic eddy in the northwest Pacific. Front. Mar. Sci. 8. https://doi.org/10.3389/fmars.2021.766544, 2022.

Dunne, J. P., Armstrong, R. A., Gnanadesikan, A., and Sarmiento, J. L.: Empirical and mechanistic models for the particle export ratio, Global Biogeochem. Cycles, 19, GB4026, https://doi.org/10.1029/2004GB002390, 2005.

Dunne, J. P., Sarmiento, J. L., and Gnanadesikan, A.: A synthesis of global particle export from the surface ocean and cycling through the ocean interior and on the seafloor, Global Biogeochem. Cy., 21, GB4006, https://doi.org/10.1029/2006GB002907, 2007.

Dunne, J. P., John, J. G., Adcroft, A. J., Griffies, S. M., Hallberg, R. W., Shevliakova, E., Stouffer, R. J., Cooke, W., Dunne, K. A., Harrison, M. J., Krasting, J. P., Malyshev, S. L., Milly, P. C. D., Phillipps, P. J., Sentman, L. T., Samuels, B. L., Spelman, M. J., Winton, M., Wittenberg, A. T., and Zadeh, N.: GFDL's ESM2 Global Coupled Climate–Carbon Earth System Models. Part I: Physical Formulation and Baseline Simulation Characteristics, J. Climate, 25, 6646–6665, https://doi.org/10.1175/jcli-d11-00560.1, 2012.

Egbert, G. D. and Erofeeva, S. Y.: Efficient inverse modeling of barotropic ocean tides, J. Atmos. Ocean. Technol., 19, 183–204, https://doi.org/10.1175/1520-0426(2002)019<0183:EIMOBO>2.0.CO;2, 2002.

Eyring, V., Bony, S., Meehl, G. A., Senior, C. A., Stevens, B., Stouffer, R. J., and Taylor, K. E.: Overview of the Coupled Model Intercomparison Project Phase 6 (CMIP6) experimental design and organization, Geosci. Model Dev., 9, 1937–1958, https://doi.org/10.5194/gmd-9-1937-2016, 2016.

Fairall, C. W., Bradley, E. F., Rogers, D. P., Edson, J. B., and Young, G. S.: Bulk parameterization of air-sea fluxes for tropical oceanglobal atmosphere Coupled-Ocean Atmosphere Response Experiment, J. Geophys. Res., 101, 3747–3764, https://doi.org/10.1029/95JC03205, 1996.

Fennel, K, Wilkin, J., Levin, J., Moisan, J., O'Reilly, J., and Haidvogel, D.: Nitrogen cycling in the Middle Atlantic Bight: Results from a three-dimensional model and implications for the North Atlantic nitrogen budget, Global Biogeochemical Cycles, 20(3), 2005GB002456, https://doi.org/10.1029/2005GB002456, 2006.

Hanawa, K., and Mitsudera, H.: Variation of water system distribution in the Sanriku coastal area, J. Oceanogr. Soc. Jap., 42, 435-446, https://doi.org/10.1007/BF02110194, 1987.

Hauri, C., Schultz, C., Hedstrom, K., Danielson, S., Irving, B., Doney, S. C., Dussin, R., Curchitser, E. N., Hill, D. F., and Stock, C. A.: A regional hindcast model simulating ecosystem dynamics, inorganic carbon chemistry and ocean acidification in the Gulf of Alaska, Biogeosciences, 17, 3837-3857, https://doi.org/10.5194/bg-17-3837-2020, 2020.

Hayashida, H., Kiss, A. E., Miyama, T., Miyazawa, Y., and Yasunaka, S.: Anomalous nutricline drives marked biogeochemical contrasts during the Kuroshio Large Meander. J Geophys Res (Oceans) 128:e2023JC019697, https://doi.org/10.1029/2023JC019697, 2023.

Hersbach, H., Bell, B., Berrisford, P., Hirahara, S., Horányi, A., Muñoz-Sabater, J., Nicolas, J., Peubey, C., Radu, R., Schepers, D., Simmons, A., Soci, C., Abdalla, S., Abellan, X., Balsamo, G., Bechtold, P., Biavati, G., Bidlot, J., Bonavita, M., De Chiara, G., Dahlgren, P., Dee, D., Diamantakis, M., Dragani, R., Flemming, J., Forbes, R., Fuentes, M., Geer, A., Haimberger, L., Healy, S., Hogan, R. J., Hólm, E., Janisková, M., Keeley, S., Laloyaux, P., Lopez, P., Lupu, C., Radnoti, G., de Rosnay, P., Rozum, I., Vamborg, F., Villaume, S., and Thépaut, J.-N.: The ERA5 global reanalysis, Q. J. Roy. Meteor. Soc., 146, 1999– 2049, https://doi.org/10.1002/qj.3803, 2020 Ishizu, M., Miyazawa, Y., Tsunoda, T., and Guo, X.: Seasonal variability in the inorganic ocean carbon cycle in the Northwest Pacific evaluated using a biogeochemical and carbon model coupled with and operational ocean model, Clim. Change, 162, 877-902, https://doi.org/10.1007/s10584-020-02779-2, 2020.

Ishizu, M., Miyazawa, Y., and Guo, X.: Long-term variations in ocean acidification indices in the northwest Pacific from 1993 to 2018, Clim. Change, 168, https://doi.org/10.1007/ s10584-021-03239-1, 2021.

Jin, S., Wei, Z., Wang, D., and Xu, T.: Simulated and projected SST of Asian marginal seas based on CMIP6 models, Front. Mar. Sci., 10:1178974, https://doi.org/10.3389/fmars.2023.1178974, 2023.

Jochum, M., Yeager, S., Lindsay, K., Moore, K., and Murtugudde, R.: Quantification of the feedback between phytoplankton and ENSO in the community climate system model, J. Clim., 23, 2916–2925, https://doi.org/10.1175/2010JCLI3254.1, 2009.

Jung, H. K., Rahman, S. M., Kang, C.-K., Park, S.-Y., Lee, S. H., and Park, H. J.: The influence of climate regime shifts on the marine environment and ecosystems in the East Asian Marginal Seas and their mechanism, Deep-Sea Res. II, 143, 110-120, https://doi.org/10.1016/j.dsr2.2017.06.010, 2017.

Jung, H.-C, Moon, B.-K., Lee, H., Choi, J.-H., Kim, H.-K., Park, J.-Y., Byun, Y.-H., Lim, Y.-J., and Lee, J.: Development and assessment of NEMO(v3.6) –TOPAZ(v2), a coupled global ocean biogeochemistry model, Asia-Pac. J. Atmos. Sci., 56, 411-428, https://doi.org/10.1007/s13143-019-00147-4, 2020.

Kang, X., Zhang, R.H., Gao, C., and Zhu, J.: An improved ENSO simulation by representing chlorophyll-induced climate feedback in the NCAR community earth system model, Sci. Rep., 7, 1-9, https://doi.org/10.1038/s41598-017-17390-2, 2017.

Kawai., H.: Hydrography of Kuroshio extension, in: Kuroshio: Its Physical Aspects, edited by: Stommel, H. and Yoshida, K., University of Tokyo Press, 235–352, 1972.

Kim, G.E., Gnanadesikan, A., and Pradal, M.A.: Increased surface ocean heating by colored detrital matter (CDM) linked to greater Northern Hemisphere ice formation in the GFDL CM2MC ESM. J. Climate, 29(24), 9063–9076. https://doi.org/10.1175/ jcli-d-16-0053.1, 2016.

Kuroda, H., Toya, Y., Watanabe, T., Nishioka, J., Hasegawa, D., Taniuchi, Y., and Kuwata, A.: Influence of Coastal Oyashio water on massive spring diatom blooms in the Oyashio area of the North Pacifc, Ocean. Prog Oceanogr., 175, 328–344. https://doi.org/10.1016/j.pocean.2019.05.004, 2019.

Kwon, K.M.: A numerical experiment on the currents along the eastern boundary of the Yellow Sea in summer 2007. M.D Thesis, Kunsan National University, 89p.

Large, W. G., McWilliams, J. C., and Doney, S. C.: Ocean vertical mixing: a review and a model with a nonlocal boundary layer parameterization, Rev. Geophys., 32, 363–403, https://doi.org/10.1029/94RG01872, 1994.

Laufkötter, C., Vogt, M., Gruber, N., Aita-Noguchi, M., Aumont, O., Bopp, L., Buitenhuis, E., Doney, S. C., Dunne, J., Hashioka, T., Hauck, J., Hirata, T., John, J., Le Quèrè, C., Lima, I. D., Nakano, H., Seferian, R., Totterdell, I., Vichi, M., and Völker, C.: Drivers and uncertainties of future global marine primary production in marine ecosystem models, Biogeosciences, 12, 6955-6984, https://doi.org/10.5194/bg-12-6955-2015, 2015.

Lauvset, S. K., Key, R. M., Olsen, A., van Heuven, S., Velo, A., Lin, X., Schirnick, C., Kozyr, A., Tanhua, T., Hoppema, M., Jutterström, S., Steinfeldt, R., Jeansson, E., Ishii, M., Perez, F. F., Suzuki, T., and Watelet, S.: A new global interior ocean mapped climatology: the 1° × 1° GLODAP version 2, Earth Syst. Sci. Data, 8, 325–340, https://doi.org/10.5194/essd-8-325-2016, 2016.

Lee, D.-G., Oh, J.-H., Noh, K. M., Kwon, E. Y., Kim, Y. H., and Kug, J.-S.: What controls the future phytoplankton change over the Yellow and East China Seas under global warming?, Front. Mar. Sci., 10:1010341, https://doi.org/10.3389/fmars.2023.1010341, 2023.

Lee, H., Moon, B.-K., Jung, H.-C., Park, J.-Y., Shim, S., La, N., Kim, A.-H., Yum, S.S., Ha, J.-C., Byun, Y.-H., Sung, H.M., and Lee, J.: Development of the UKESM-TOPAZ Earth System Model (Version 1.0) and preliminary evaluation of its biogeochemical simulations, Asia-Pac. J. Atmos. Sci., 58(3), 379-400, https://doi.org/10.1007/s13143-021-00263-0, 2022.

Lembke-Jene, L, Tiedemann, R., Nürnberg, D., Kokfelt, U., Kozdon, R., Max, L., Röhl, U., and Gorbarenko, A.: Deglacial variability in Okhotsk Sea Intermediate Water ventilation and biogeochemistry: Implications for North Pacific nutrient supply and productivity, Quat. Sci. Rev., 160, 116-137, https://doi.org/10.1016/j.quascirev.2017.01.016, 2017.

Ma, S., Tian, Y., Li, J., Yu, H., Cheng, J., Sun, P., Fu, C., Liu, Y., and Watanabe, Y.: Climate variability patterns and their ecological effects on ecosystems in the Northwestern North Pacific, Front. Mar. Sci., 7, 546882, https://doi.org/10.3389/fmars.2020.546882, 2020.

Mauri, E., Poulain, P., Juznic-Zonta, Z.: MODIS chlorophyll variability in the northern Adriatic Sea and relationship with forcing parameters, J. Geophys. Res., 112, 1–14, https://doi.org/10.1029/2006JC003545, 2007

Manizza, M., Le Quéré, C., Watson, A.J., Buitenhuis, E.T.: Bio-optical feedbacks among phytoplankton, upper ocean physics and sea-ice in a global model. Geophys. Res. Lett. 32, L05603, https://doi.org/10.1029/2004GL020778, 2005.

McWilliams, J. C.: Targeted coastal circulation phenomena in diagnostic analyses and forecast, Dynam. Atmos. Oceans, 49, 3–15, https://doi.org/10.1016/j.dynatmoce.2008.12.004, 2009.

Mellor, G. L. and Yamada, T.: Development of a turbulence closure model for geophysical fluid problems, Rev. Geophys., 20, 851– 875, https://doi.org/10.1029/RG020i004p00851, 1982.

Moon, J.H., Hirose, N., and Yoon, J.-H.: Comparison of wind-tidal contributions to seasonal circulation of the Yellow Sea, J. Geophys. Res., 114, https://doi.org/10.1029/2009JC005314, 2009.

Na, R., Rong, Z., Wang, Z.A., Liang, S., Liu, C., Ringham, M., and Liang, H.: Air-sea CO_2 fluxes and cross-shelf exchange of inorganic carbon in the East China Sea from a coupled physical-biogeochemical model, Sci. Total Environ., 906, 167572, https://doi.org/10.1016/j.scitotenv.2023.167572, 2024.

Najjar, R. and Orr, J. C.: Design of OCMIP-2 simulations of chlorofluorocarbons, the solubility pump and common biogeochemistry, Internal OCMIP Report, LSCE/CEA Saclay, Gif-surYvette, France 1998.

Nishioka, J., Obata, H., Ogawa, H., Ono, K., Yamashita, Y., Lee, K., Takeda, S., and Yasuda, I.: Subpolar marginal seas fuel the Norh Pacific through the intermediate water at the termination of the global ocean circulation, P. Natl. Acad. Sci. USA, 117, 12665–12673, https://doi.org/10.1073/pnas.2000658117, 2020.

Nishioka, J., Obata, H., Hirawake, T., Kondo, Y., Yamashita, Y., Misumi, K., and Yasuda, I.: A review: iron and nutrient supply in the subarctic Pacific and its impact on phytoplankton production, J. Oceanogr., 77, 561-587, https://doi.org/10.1007/s10872-021-00606-5, 2021.

Nitani, H.: Beginning of the Kuroshio, in: Kuroshio: Its Physical Aspects, edited by: Stommel, H. and Yoshida, K., University of Tokyo Press, 129–163, 1972.

Overland, J., Rodionov, S., Minobe, S., and Bond, N.: North Pacific regime shifts: definitions, issues and recent transitions, prog, oceanogr., 77, 92-102, https://doi.org/10.1016/j.pocean.2008.03.016, 2008.

Qui, B.: Kuroshio and Oyashio currents, in: edited by Steele, J. H., Thorpe, S. A., Turekian, K. K., Encyclopedia of Ocean Sciences. Academic, London, 1413-1425, https://doi.org/10.1006/rwos.2001.0350, 2001

Park, J.-Y., Kug, J.-S., Seo, H., and Bader, J.: Impact of bio-physical feedbacks on the tropical climate in

779   coupled and uncoupled GCMs, Clim. Dyn., 43, 1811-1827, https://doi.org/10.1007/s00382-013-2009-0, 2014.

780   Park, J.-Y., Dunne, J.P., and Stock, C.A.: Ocean chlorophyll as a precursor of ENSO: An Earth system modeling
781   study, Geophys. Res. Lett., 45, 1939-1947, https://doi.org/10.1002/2017GL076077, 2018.

782   Park, J.-Y., Stock, C.A., Dunne, J.P., Yang, X., and Rosati, A.: Seasonal to multiannual marine ecosystem
783   prediction with a global earth system model. Science, 365, 284-288, DOI: 10.1126/science.aav6634, 2019.

784   Okamoto, S., Hirawake, T., and Saito, S.: Internal variability in the magnitude and timing of the spring bloom in
785   the Oyashio region, Deep Sea Res. II, 57, 1608-1617, https://doi.org/10.1016/j.dsr2.2010.03.005, 2010.

786   Reid, P.C., Fischer, A.C., Lewis-Brown, E., Meredith, M.P., Sparrow, M., Andersson, A.J., Antia, A., Bates,
787   N.R., Bathmann, U., Beaugrand, G., Brix, H., Dye, S., Edwards, M., Furevik, T., GangstØ, R., Hátún, H.,
788   Hopcroft, R.R., Kendall, M., Kasten, S., Keeling, R., Le Qur, C., Mackenzie, F.T., Malin, G., Mauritzen, C.,
789   Olafsson, J., Paull, C., Rignot, E., Shimada, K., Vogt, M., Wallace, C., Wang, Z., and Washington, R.: Chapter
790   1 Impacts of the Oceans on Climate Change. Academic Press, 56, 1-150, https://doi.org/10.1016/S0065-
791   2881(09)56001-4, 2009.

792   Séférian, R., Gehlen, M., Bopp, L., Resplandy, L., Orr, J.C., Marti, O., Dunne, J.P., Christian, J.R., Doney, S.C.,
793   Ilyina, T., Lindsay, K., Halloran, P.R., Heinze, C., Segschneider, J., Tjiputra, J., Aumont, O., and Romanou,
794   A.: Inconsistent strategies to spin up models in CMIP5: implications for ocean biogeochemical model
795   performance assessment. Geosci. Model Dev. 9, 1827–1851, https://doi.org/10.5194/gmd-9-1827-2016, 2016.

796   Shchepetkin, A. F. and McWilliams, J. C.: A method for computing horizontal pressure-gradient force in an
797   oceanic model with a nonaligned vertical coordinate, J. Geophys. Res., 108, 3090,
798   https://doi.org/10.1029/2001JC001047, 2003.

799   Shchepetkin, A. F. and McWilliams, J. C.: The regional oceanic modeling system (ROMS): a split-explicit, free-
800   surface, topography-following-coordinate oceanic model, Ocean Model., 9, 347–404,
801   https://doi.org/10.1016/j.ocemod.2004.08.002, 2005.

802   Shiozaki, T., Ito, S.-I., Takahashi, K., Saito, H., Nagata, T., and Furuya, K.: Regional variability of factors
803   controlling the onset timing and magnitude of spring algal blooms in the northwestern North Pacific, J.
804   Geophys. Res., 119, 253-265, https://doi. org/10.1002/2013JC009187, 2014.

805   Siswanto, E., Matsumoto, K., Honda, M. C., Fujiki, T., Sasaoka, K. and Saino, T.: Reappraisal of meridional
806   differences of factors controlling phytoplankton biomass and initial increase preceding seasonal bloom in the
807   northwestern Pacific Ocean. Remote Sensing of Envir., 159, 44-56, https://doi.org/10.1016/j.rse.2014.11.028,
808   2015.

809   Song, Y., and Haidvogel, D.: A semi-implicit ocean circulation model using a generalized topography following
810   coordinate system, J. Comput. Phys., 115, 228-244, https://doi.org/10.1006/jcph.1994.1189, 1994.

811   Song, Y. T. and Wright, D. G.: A general pressure gradient formulation for ocean models, Part II: Energy,
812   momentum, and bottom torque consistency, Mon. Weather Rev., 126, 3231–3247,
813   https://doi.org/10.1175/1520-0493(1998)126<3231:AGPGFF>2.0.CO;2, 1998.

814   Sugimoto, S., and Hanawa, K.: Roles of SST anomalies on the wintertime turbulent heat fluxes in the Kuroshio–
815   Oyashio confluence region: influences of warm eddies detached from the Kuroshio extension. J Clim.
816   https://doi.org/10.1175/2011jcli4023.1, 2011.

817   Taguchi, B., Xie, S.-P., Schneider, N., Nonaka, M., Sasaki, H., and Sasai, Y.: Decadal variability of the Kuroshio
818   Extension: Observations and an eddy-resolving model hindcast, J. Climate, 20, 2357–2377,
819   https://doi.org/10.1175/JCLI4142.1, 2007.

820   Takahashi, T., Sutherland, S. C., Wanninkhof, R., Sweeney, C., Feely, R. A., Chipman, D. W., Hales, B.,
821   Friederich, F., Chavez, F., Sabine, C., Watson, A., Bakker, D. C.E., Schuster, U., Metzl, N., Yoshikawa-Inoue,
822   H., Ishii, M., Midorikawa, T., Nojiri, Y., KÖrtzinger, A., Steinhoff, T., Hoppema, M., Olafsson, J., Arnarson,
823   T. S., Tilbrook, B., Johannessen, T., Olsen, A., Bellerby, R., Wong, C.S., Delille, B., Bates, N.R., and de Baar,
824   H. J.W.: Climatological mean and decadal change in surface ocean pCO2, and net sea-air CO2 flux over the
825   global oceans, Deep-Sea Res. II, 56, 554-577, 2009.

826   Taniguchi, A.: Differences in the structure of the lower trophic levels of pelagic ecosystems in the eastern and

827   western subarctic Pacific, Prog. in Oceanogra., 43, 289-315, https://doi.org/10.1016/S0079-6611(99)00011-7,
828   1999.

829   Taylor, K.E.: Summarizing multiple aspects of model performance in a single diagram, J. Geophys. Res.-Atmos.
830   106, 7183–7192, https://doi.org/10.1029/2000JD900719, 2001.

831   Taylor, K., Juckes, M., Balaji, V., Cinquini, L., Denvil, S., Durack, P., Elkington, M., Guilyardi, E., Kharin, S.,
832   Lautenschlager, M., Lawrence, B., Nadeau, D., and Stockhause, M.: CMIP6 Global Attributes, DRS,
833   Filenames, Directory Structure, and CV's, https://github.com/WCRP-CMIP/WGCM_Infrastructure_Panel/
834   blob/main/Papers/CMIP6_global_attributes_filenames_CVs_ v6.2.7.pdf (last access: 15 January 2021), 2018.

835   Umlauf, L., Burchard, H., and Hutter, K.: Extending the κ-ω turbulence model towards oceanic applications,
836   Ocean Model., 5, 195–218, 5. https://doi.org/10.1357/00222 4003322005087, 2003.

837   Wang, X., Luo, C., Ge, T., Xu, C., and Xum Y.: Controls on the sources and cycling of dissolved inorganic
838   carbon in the Chanjiang and Huanghe River estuaries, China: ^{14}C and ^{13}C studies, Limnol. And Oceanogra.,
839   61, 1358-1374, https://doi.org/10.1002/lno.10301, 2016.

840   Wang, Y., Kang, J., Sun, X., Huang, J., Lin, Y., and Xiang, P.: Spatial patterns of phytoplankton community and
841   biomass along the Kuroshio extension and adjacent water in late spring, Mar. Biol.,
842   https://doi.org/10.1007/s00227-021-03846-7, 2021.

843   Wang, Y., Bi, R., Zhang, J., Gao, J., Takeda, S., Kondo, Y., Chen, F., Jin, G., Sachs, J. P., and Zhao, M.:
844   Phytoplankton distributions in the Kuroshio-Oyashio Region of the Northwest Pacific Ocean: Implications for
845   marine ecology and carbon cycle, Front. Mar. Sci., 9, 865142, https://doi.org/10.3389/fmars.2022.865142,
846   2022.

847   Wanninkhof, R.: Relationship between wind speed and gas exchange over the ocean. J. Geophys. Res. 97, 7373–
848   7382m https://doi.org/10.1029/92JC00188, 1992.

849   Watson A. J.: Iron limitation in the oceans. In The Biogeochemistry of Iron in Seawater, Turner DR, Hunter KA
850   (eds). Wiley: Chichester; 9–39, 2001.

851   Weatherall, P., Marks, K. M., Jakobsson, M., Schmitt, T., Tani, S., Arndt, J. E., Rovere, M., Chayes, D., Ferrini,
852   V., and Wigley, R.: A new digital bathymetric model of the world's oceans, Earth Space Sci., 2, 331–345,
853   https://doi.org/10.1002/2015EA000107, 2015.

854   Wu, Q., Wang, X., He, Y., and Zheng, J.: The relationship between chlorophyll concentration and ENSO events
855   and possible mechanisms off the Changjiang River estuary, Remote Sens., 15, 2384,
856   https://doi.org/10.3390/rs15092384, 2023.

857   Yasuda, I.: Hydrographic structure and variability in the Kuroshio–Oyashio transition area, J. Oceanogr., 59,
858   389–402, https://doi.org/10.1023/A: 1025580313836, 2003.

859   Yatsu, A., Chiba, S., Yamanaka, Y., Ito, S., Shimizu, Y., and Kaeriyama, M.: Climate forcing and the
860   Kuroshio/Oyashio ecosystem, ICES J. Mar. Sci., 70, 922-933, https://doi.org/10.1093/icesjms/fst084, 2013.

861   Zhai, W.-D., Dai, M.-H., and Guo, X.-H.: Carbonate system and CO_2 degassing fluxes in the inner estuary of
862   Changjiang (Yangtze) River, China. Mar. Chem., 107, 342-356,
863   https://doi.org/10.1016/j.marchem.2007.02.011, 2007.

864   Zhang, H.-R., Wang, Y., Xiu, P., Qi, Y., and Chai, F. (2021b). Roles of iron limitation in phytoplankton dynamics
865   in the Western and Eastern subarctic pacific, Front. Mar. Sci., 8. https://doi.org/10.3389/fmars.2021.735826,
866   2021.

867   Zhao, H., Dai, M., Gan, J., Zhao, X., Lu, Z., Liang, L., Liu, Z., Su, J., and Cao, Z.: River-dominated pCO_2
868   dynamics in the northern South China Sea during summer: A modeling study, Prog. Oceanogr., 190, 102457,
869   https://doi.org/10.1016/j.pocean.2020.102457, 2021.

870   Zhu, K., Chen, X., Mao, K., Hu, D., Hong, S., and Li, Y.: Mixing characteristics of the subarctic front in the
871   Kuroshio-Oyashio confluence region. Oceanologia., 61, 103–113,
872   https://doi.org/10.1016/j.oceano.2018.07.004, 2019.

873   Zhou, M.J., Shen, Z.L., and Yu, R.C.: Responses of a coastal phytoplankton community to increased nutrients
874   input from the Changjiang (Yangtze) River, Cont. Shelf Res., 28, 1483-1489,

875   https://doi.org/10.1016/j.csr.2007.02.009, 2008.

876

877

878

879

880

881

882

883

884

885

886

887

888

889
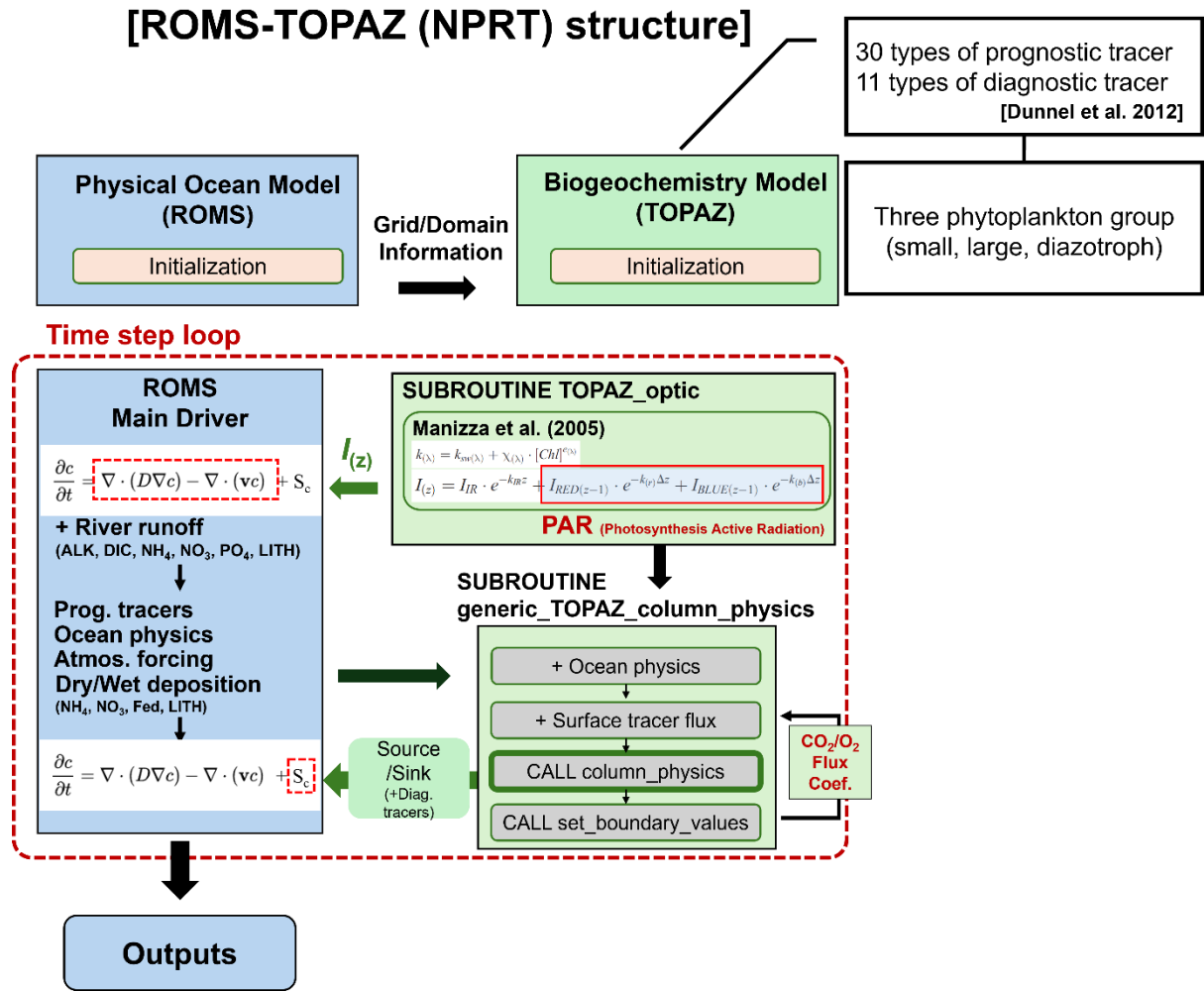
Fig. 1. Flow diagram of the ROMS–TOPAZ model (NPRT). Blue (green) boxes represent the
ocean physical (biogeochemical) module. The black arrows indicate the process of
transferring oceanic physical information to biogeochemical modules, and the green arrows
represent vice versa process.

894
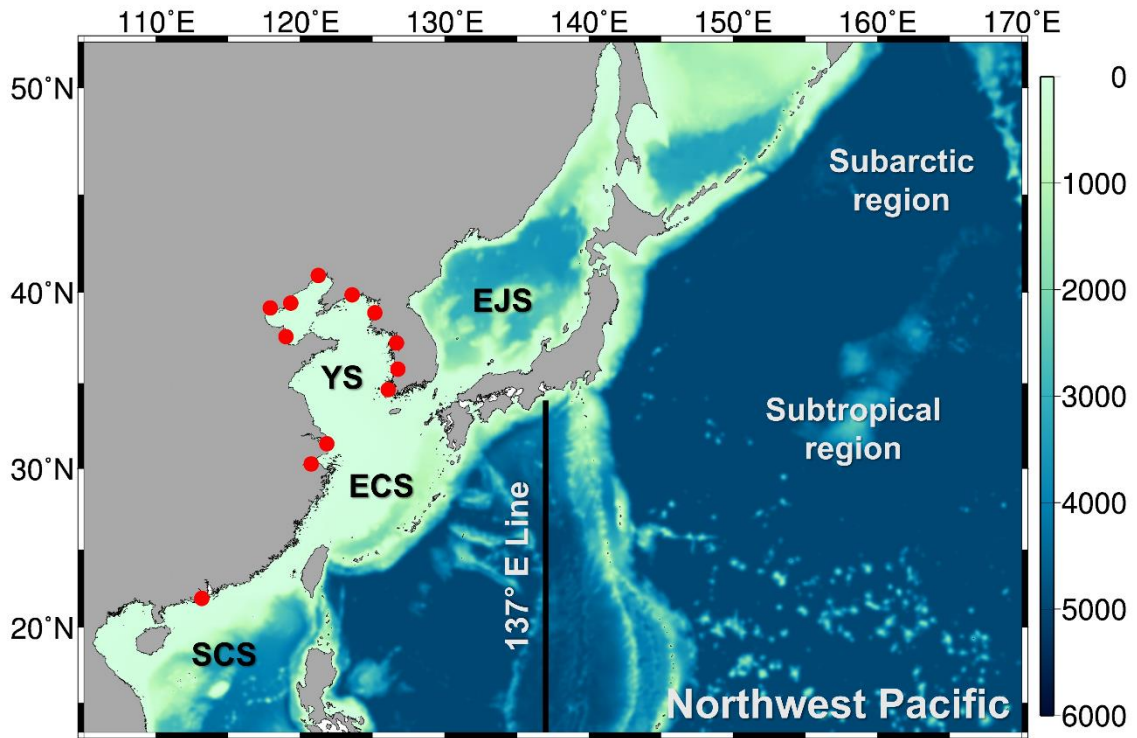
Fig. 2. Model domain and bottom topography for NPRT coupled modeling system. EJS: East/Japan Sea, YS: Yellow Sea, ECS: East China Sea, SCS: South China Sea. The red circles indicate river runoff points, and the black line (137° E line) is the observation line of the Japanese Meteorological Agency (JMA).

906
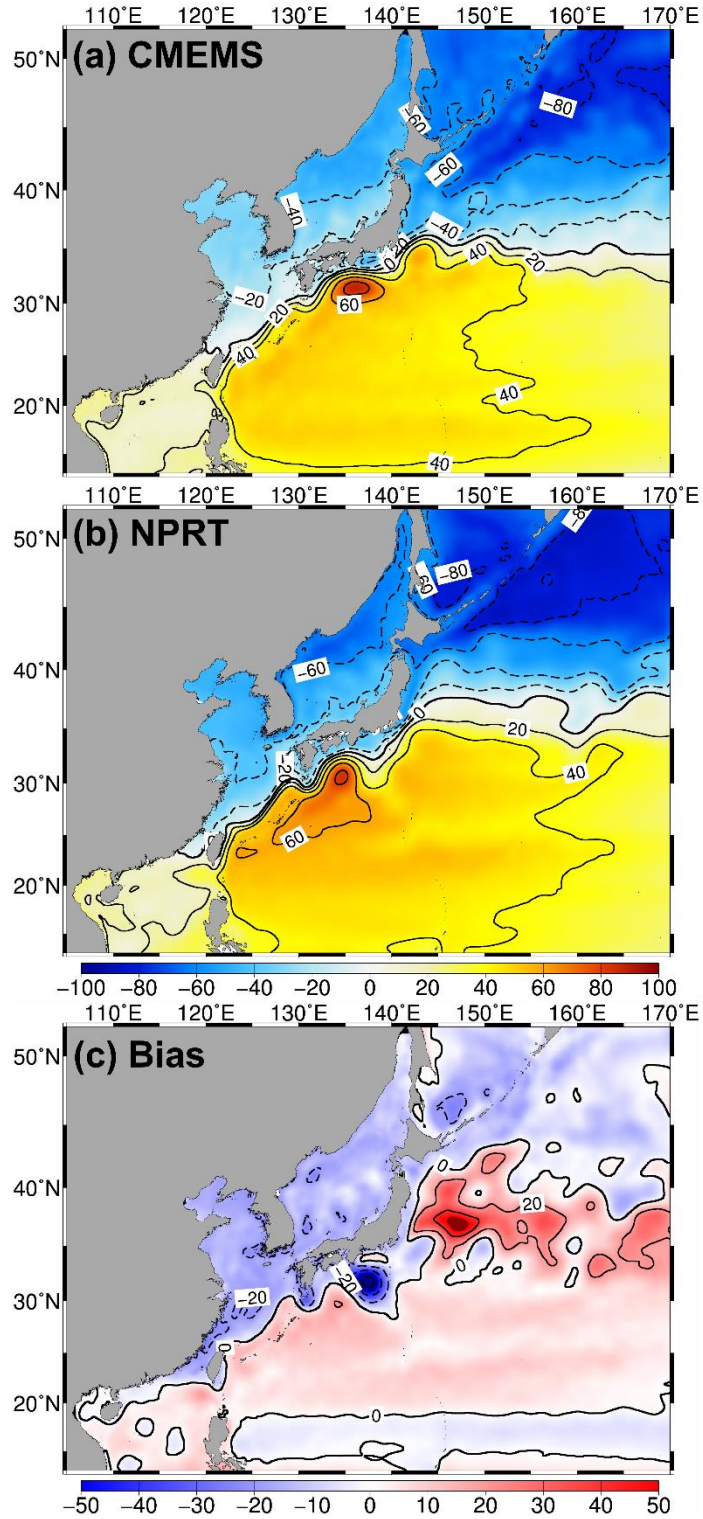
Fig. 3. Distributions of the annual mean sea surface height (SSH; cm) in (a) satellite altimeters
(CMEMS), (b) NPRT, and (c) biases between NPRT and observations (WOA18) from 2005
to 2014. To compare the two datasets, the spatial mean was subtracted from each one.

910
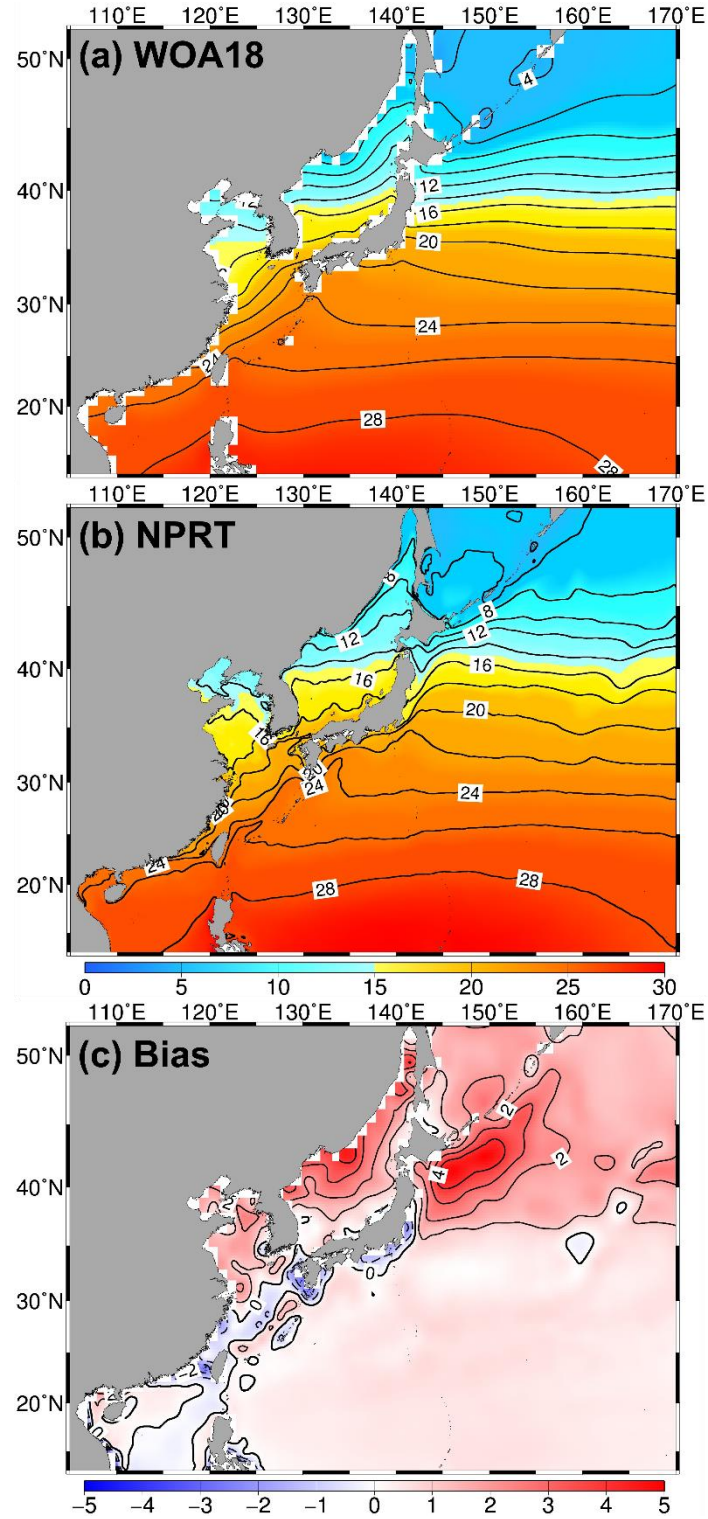
911 **Fig. 4.** Same as Fig. 3, except to in the annual mean sea surface temperature (SST) from (a)
912   World Ocean Atlas 2018 (WOA18), (b) NPRT, and (c) bias (NPRT – WOA18).

913
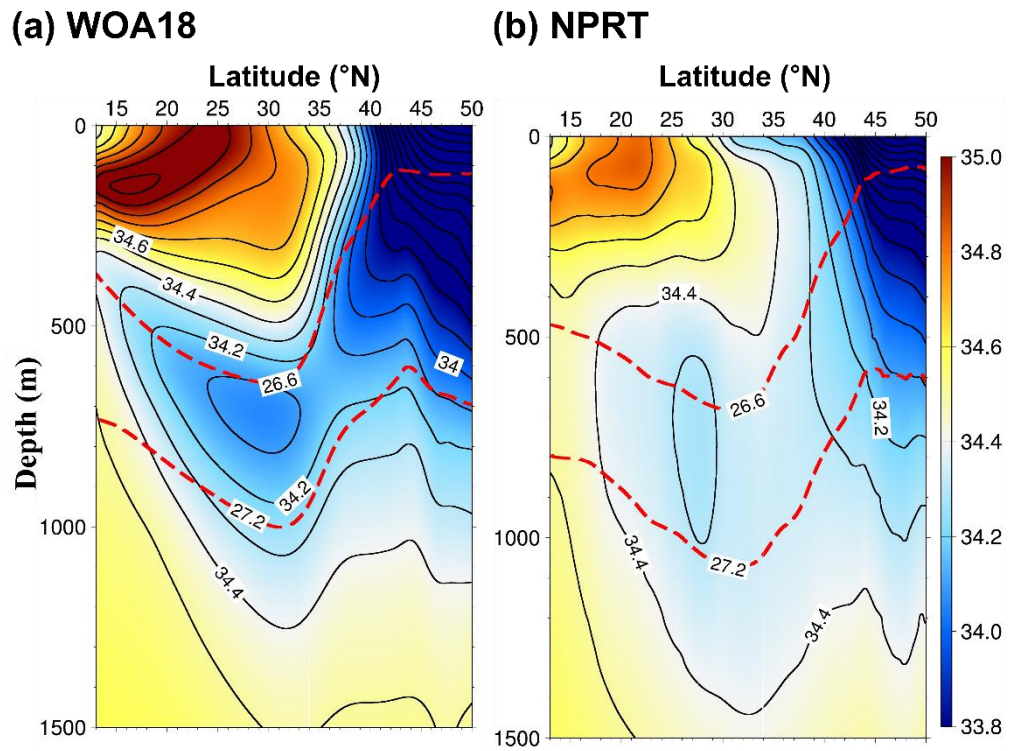
Fig. 5. Vertical structures of the climatological zonally averaged annual mean salinity between 145° E and 160° E in (a) the WOA18 data and (b) NPRT. The red dashed lines represent potential 26.6 σ_θ and 27.2 σ_θ isopycnals, corresponding to the NPIW density range.

919
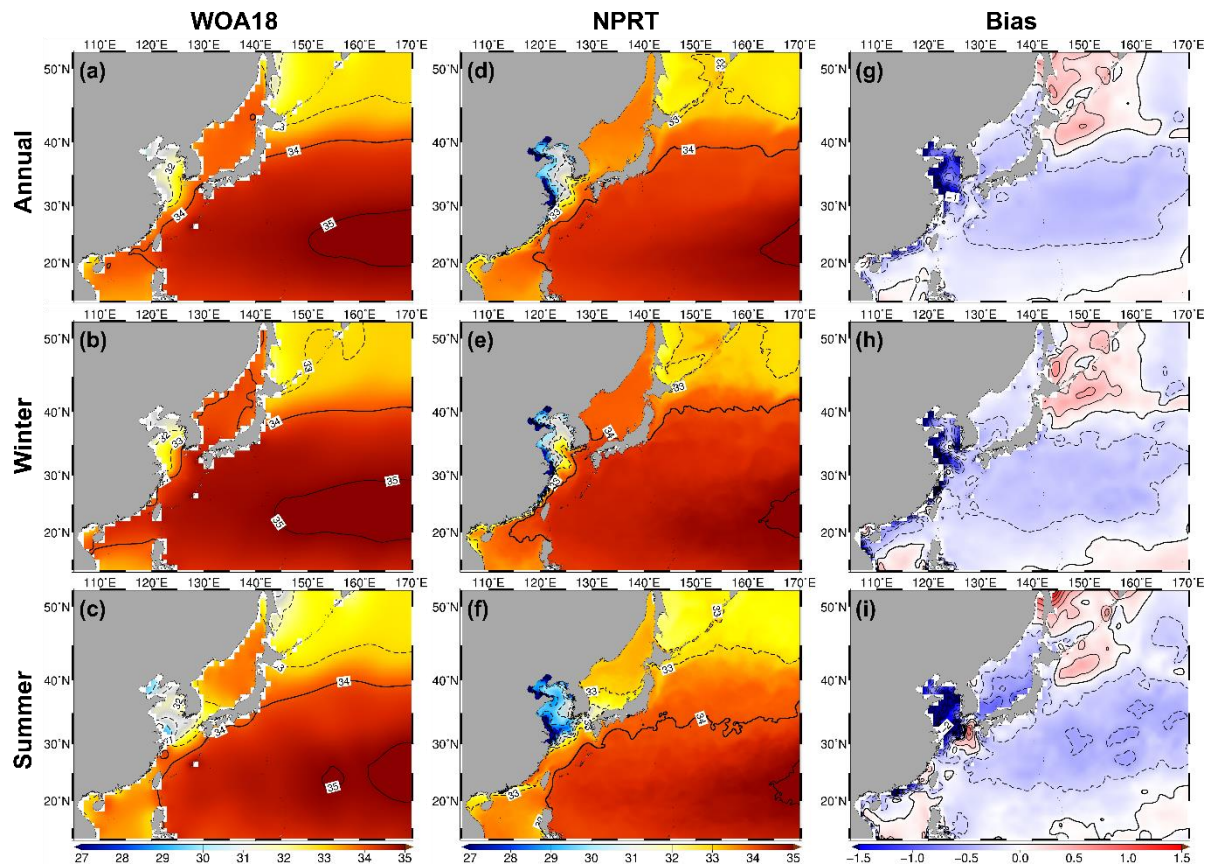
Fig. 6. Distributions of the surface salinity in (a, b, c) the WOA18 data, (d, e, f) NPRT, and (g,

h, i) biases for (a, d, g) the climatological mean, (b, e, h) winter and (c, f, i) summer.

922

923
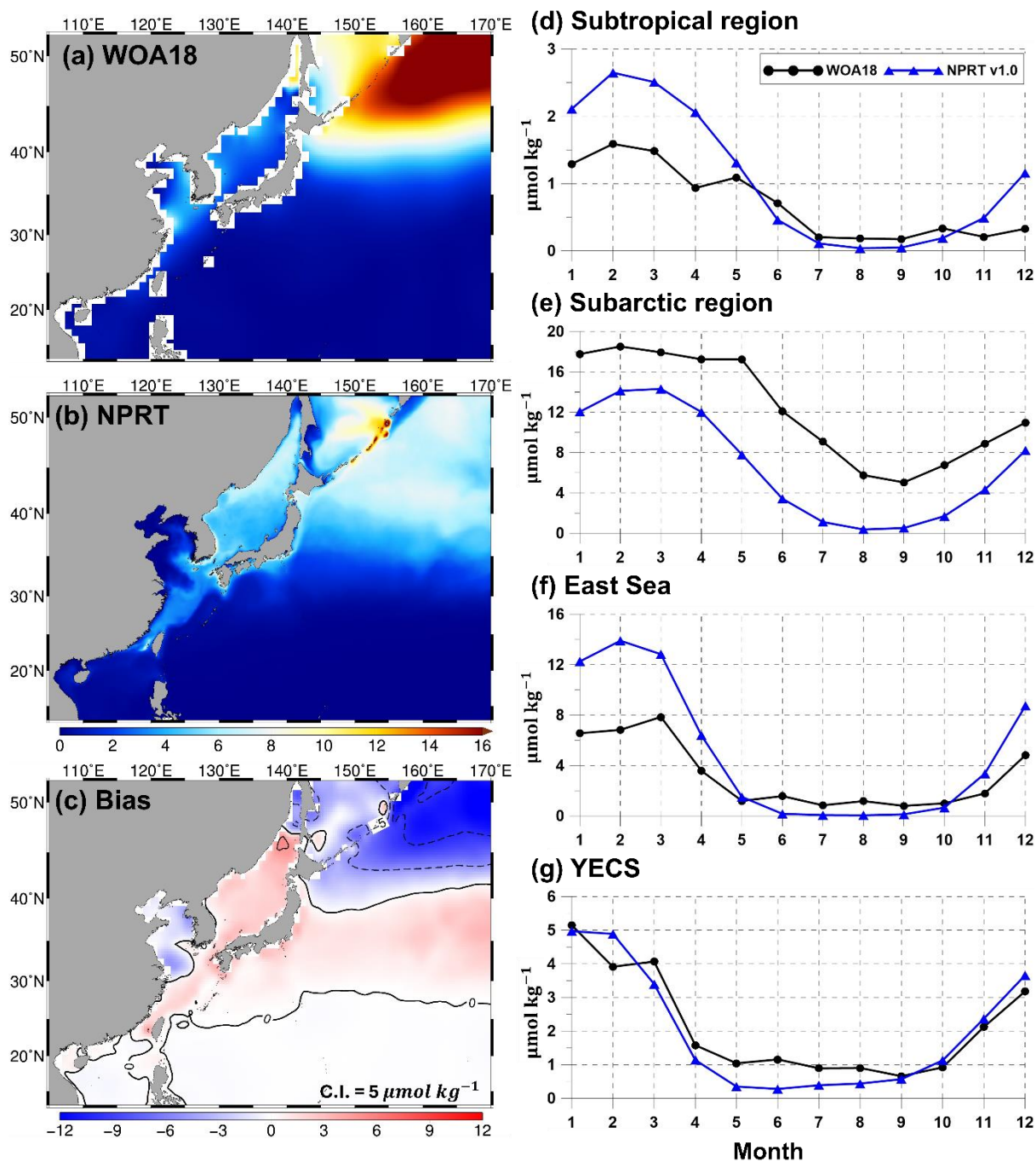
Fig. 7. Horizontal distributions of the annual mean surface nitrate concentrations (μmol kg⁻¹) in (a) WOA18, (b) NPRT, and (c) biases between NPRT and observations (WOA18), and seasonal variations in (d) the subtropical region (south of 40° N in the Northwest Pacific), (e) the subarctic region (north of 40° N in the Northwest Pacific), (f) the East Sea, and (g) the Yellow and East China Seas (YECS).

929
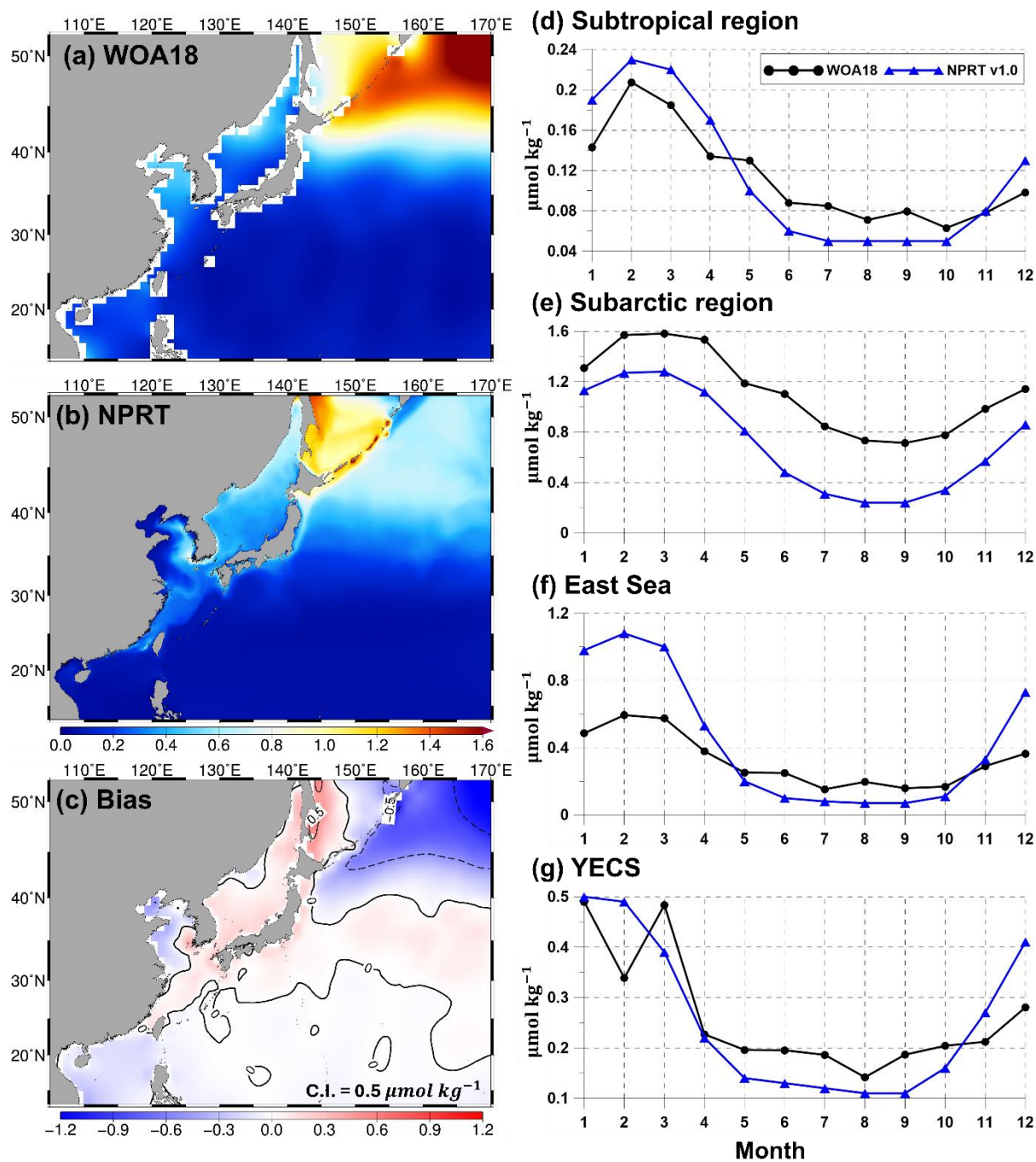
Fig. 8. Same as Fig. 7 except to the annual mean surface phosphate concentration (μmol kg⁻¹).

931

932

933

934
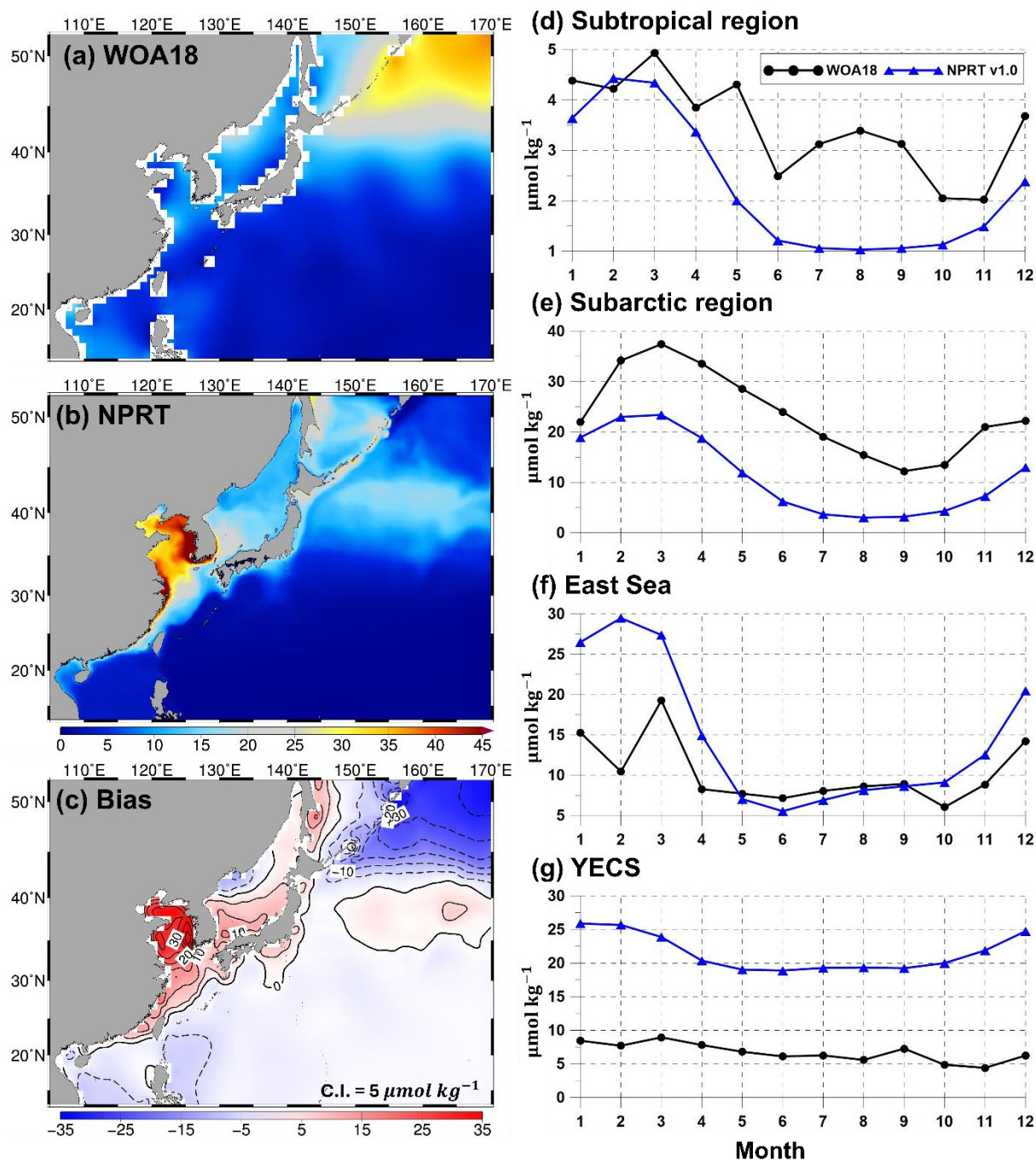
935 **Fig. 9.** Same as Fig. 7 except to the annual mean surface silicate concentration (μmol kg^{-1}).

936

937

938
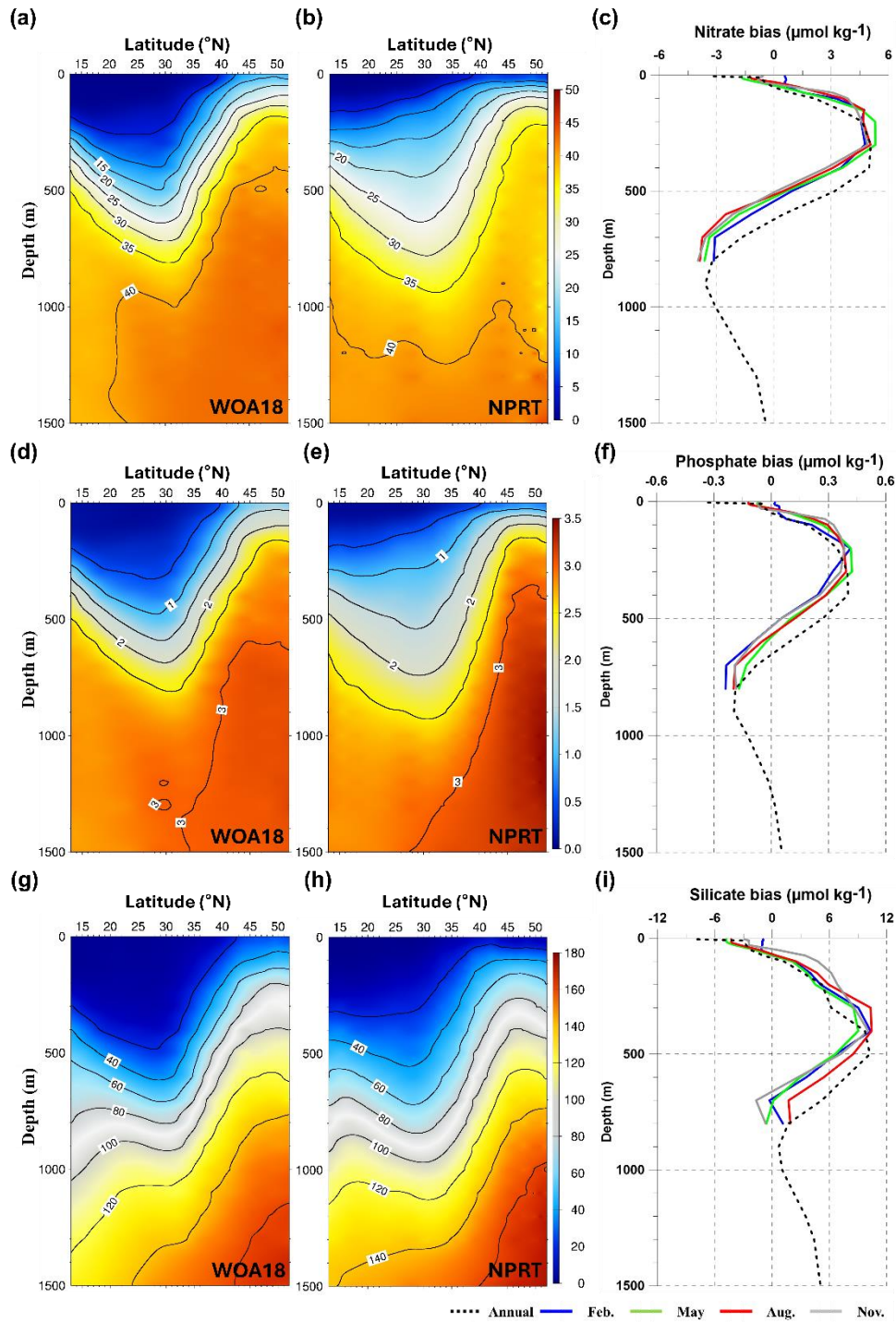
Fig. 10. Vertical structures of the zonal averaged annual mean (a, b) nitrate, (d, e) phosphate, and (g, h) silicate concentrations (µmol kg^{-1}) in the Northwest Pacific. The vertical profile of annual and monthly biases between observation and NPRT results for (c) nitrate, (f) phosphate, and (i) silicate.

943
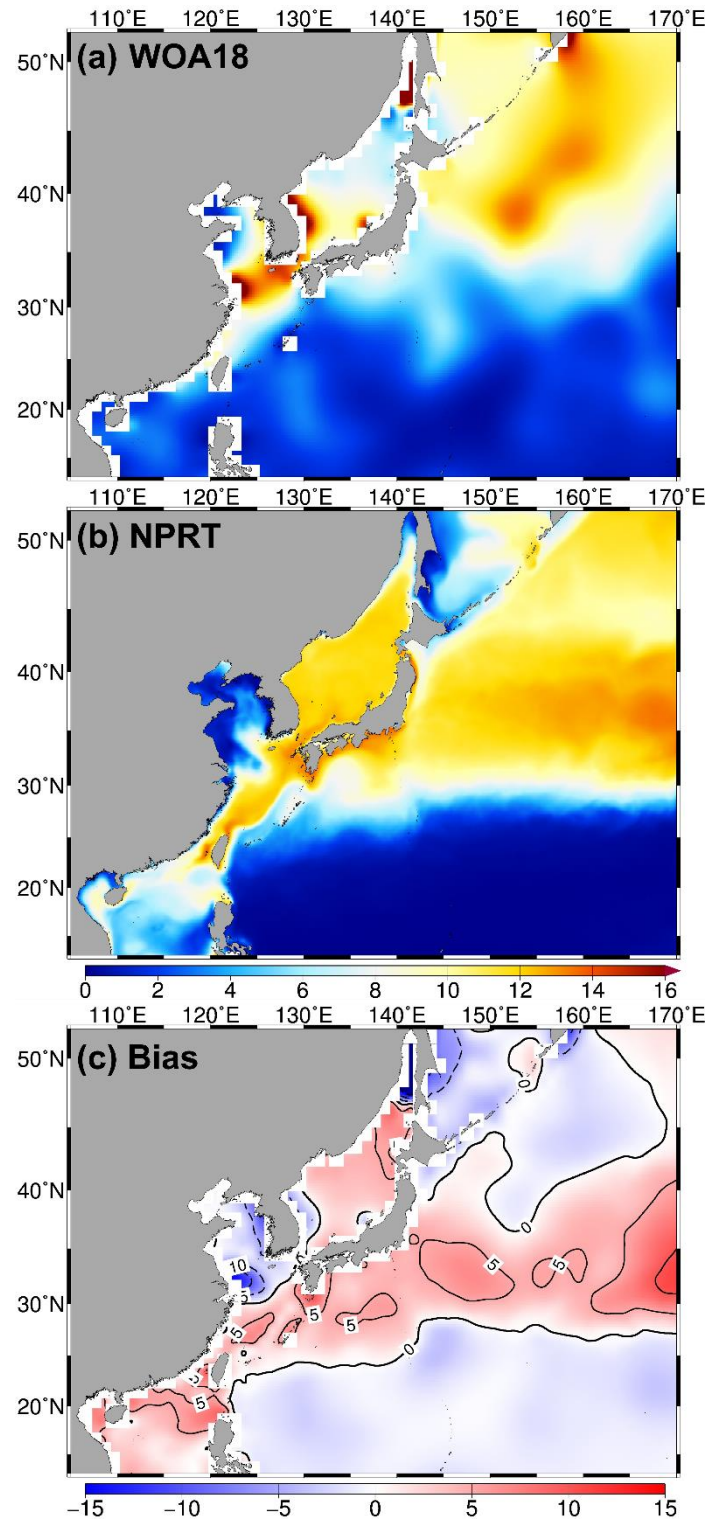
Fig. 11. Same as Fig. 3, except to in the annual mean surface N:P molar ratio.

945

946

947
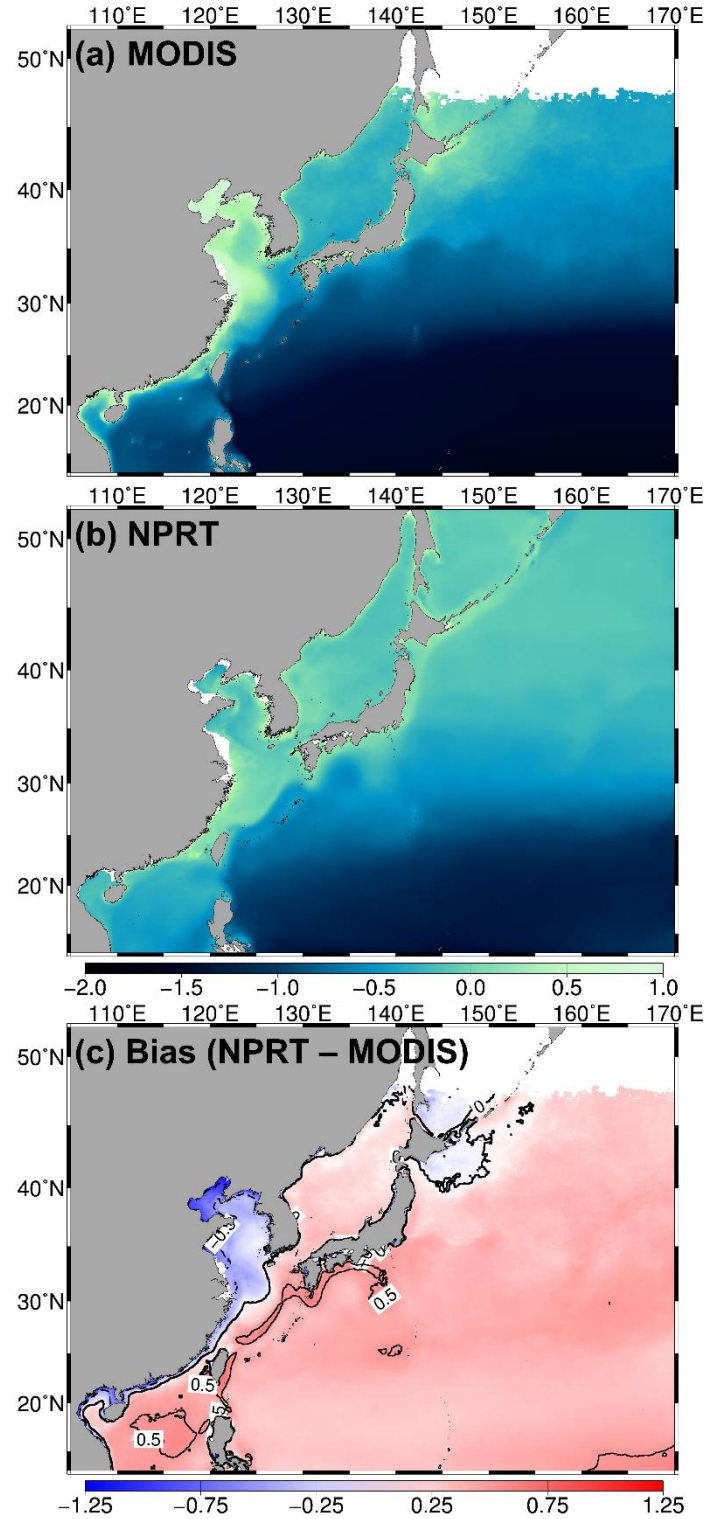
Fig. 12. Logarithm of the climatological annual-mean surface chlorophyll concentrations (μmol kg^{-1}) from (a) MODIS, (b) NPRT, (c) bias of between NPRT and observation (MODIS).

950
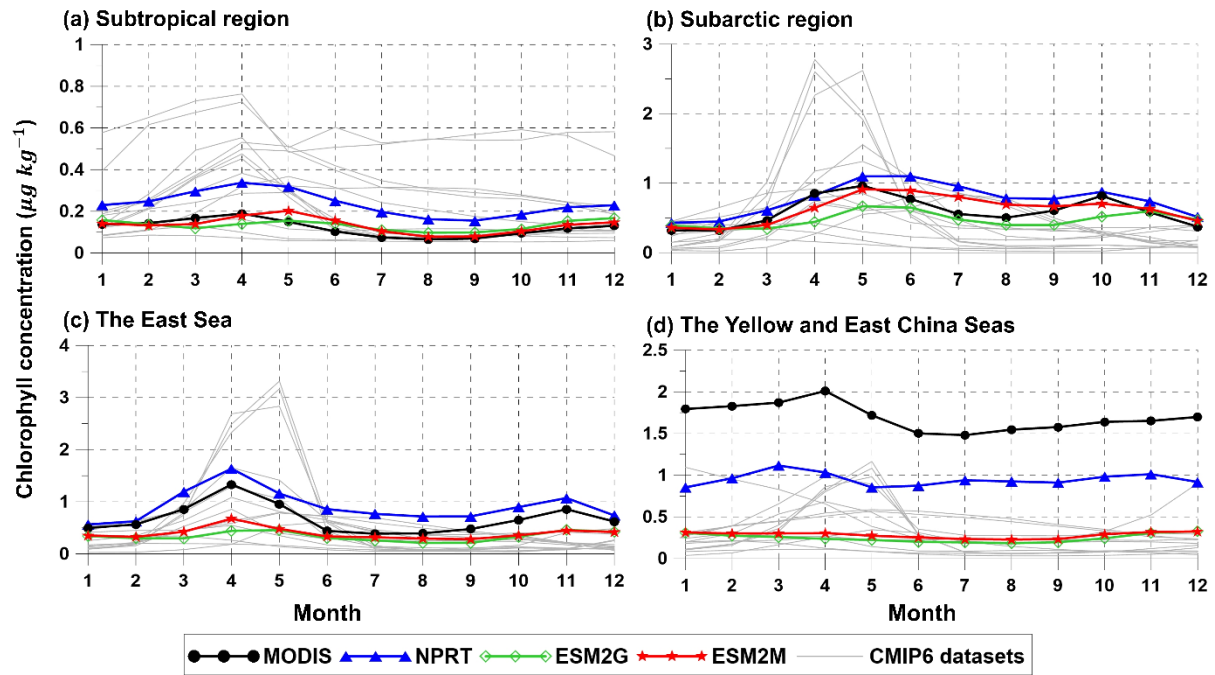
Fig. 13. Seasonal variations of the spatial averaged chlorophyll concentrations (μmol kg⁻¹) in (a) the subtropical and (b) subarctic regions, (c) the East Sea, and (d) the YECS. Black, blue, green, red and light grey lines indicate MODIS, NPRT, GFDL–ESM2G, GFDL–ESM2M, and each ensemble model in CMIP6, respectively.

955
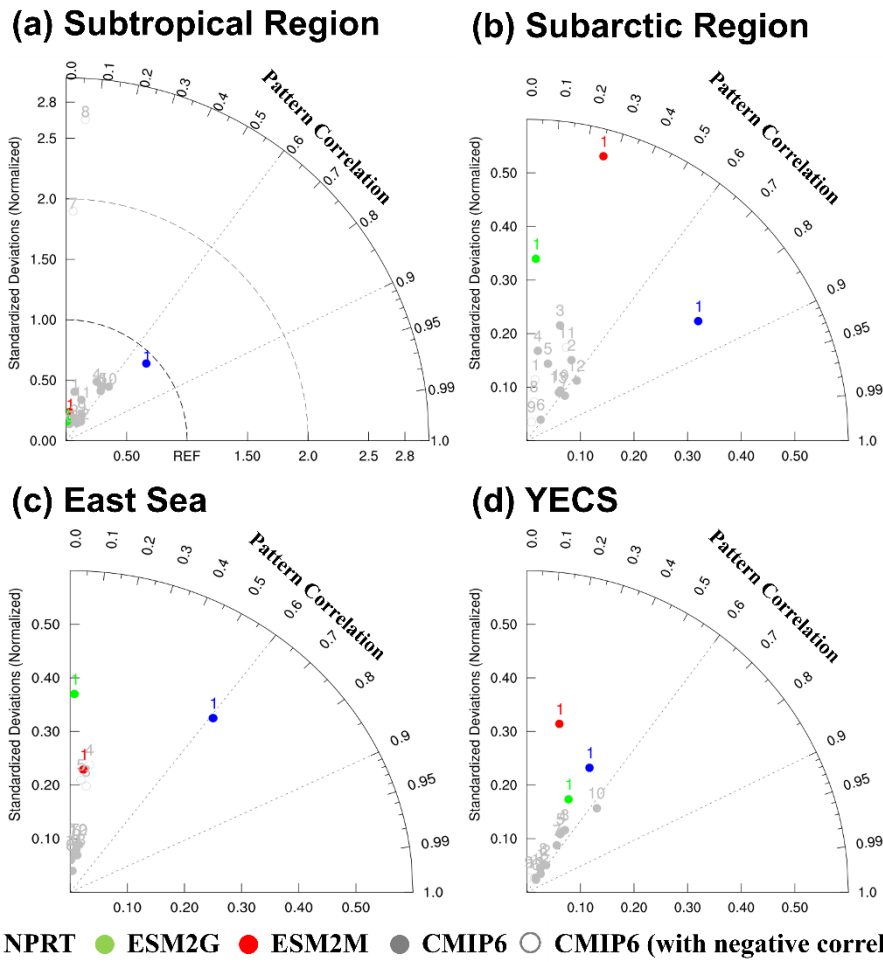
Fig. 14. Taylor diagrams (Taylor, 2001) of spatial four models (NPRT (blue dots), GFDL–ESM2G (green dots), GFDL–ESM2M (red dots) and each ensemble model in CMIP6 (grey dots)) for surface chlorophyll concentrations compared to observation (MODIS) at each region. The grey open dots (○) in CMIP6 indicate a negative pattern correlation. Taylor diagrams for time were calculated by comparing observational data with annual mean simulated fields of four models (NPRT, GFDL–ESM2G, GFDL–ESM2M and each ensemble in CMIP6) in the (a) subtropical and (b) subarctic regions, (c) East Sea, and (d) YECS, and the numbers represent each ensemble model in Table 1.

964

965
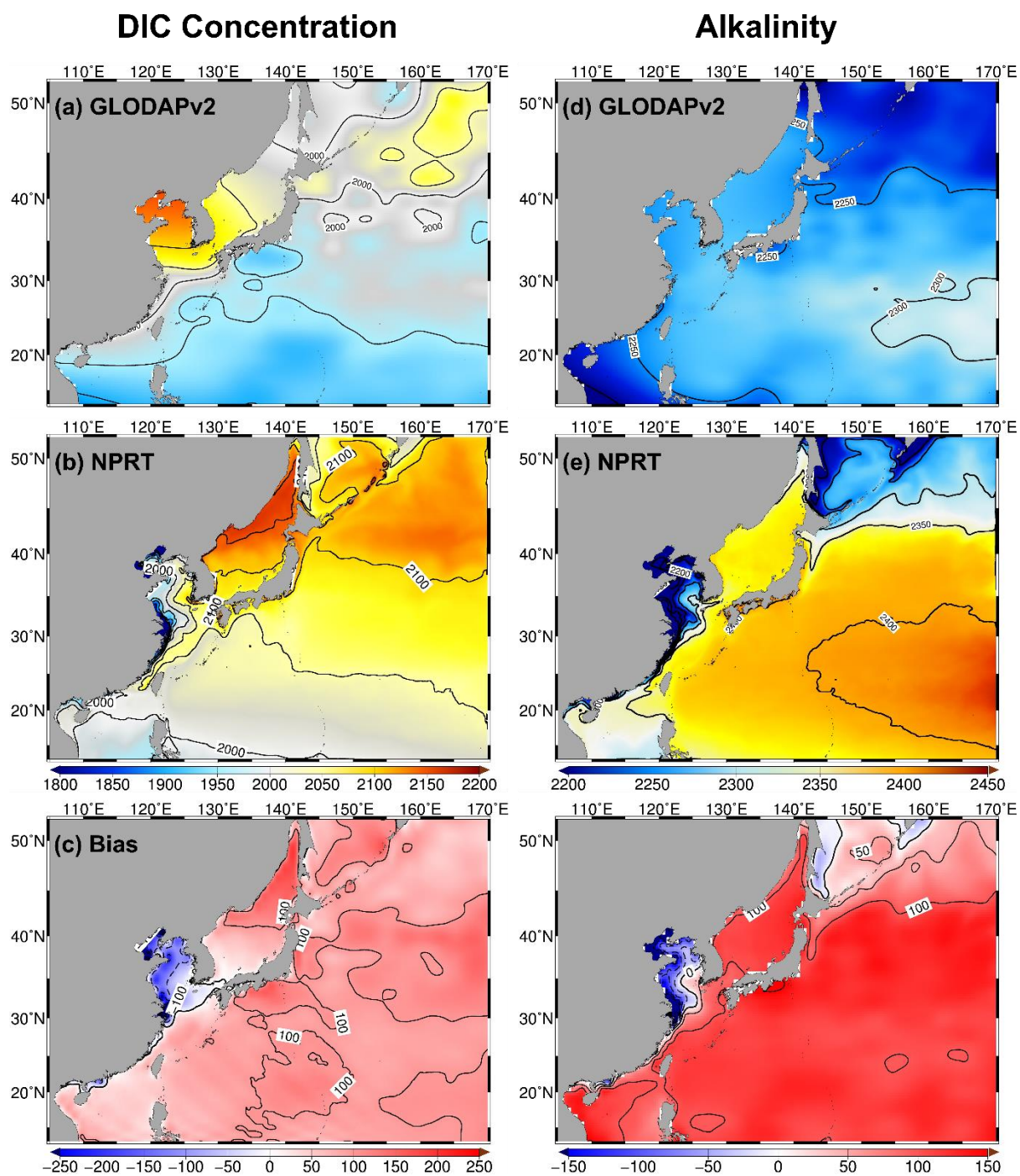
Fig. 15. Horizontal distributions of annual mean surface dissolved inorganic carbon (DIC; left panels) concentrations (µmol kg^{-1}) and alkalinity (µeq kg^{-1}; right panels) in the (a, d) GLODAPv2 and (b, e) NPRT in the Northwest Pacific. Biases (c, f) represent NPRT minus observation (GLODAPv2).

972
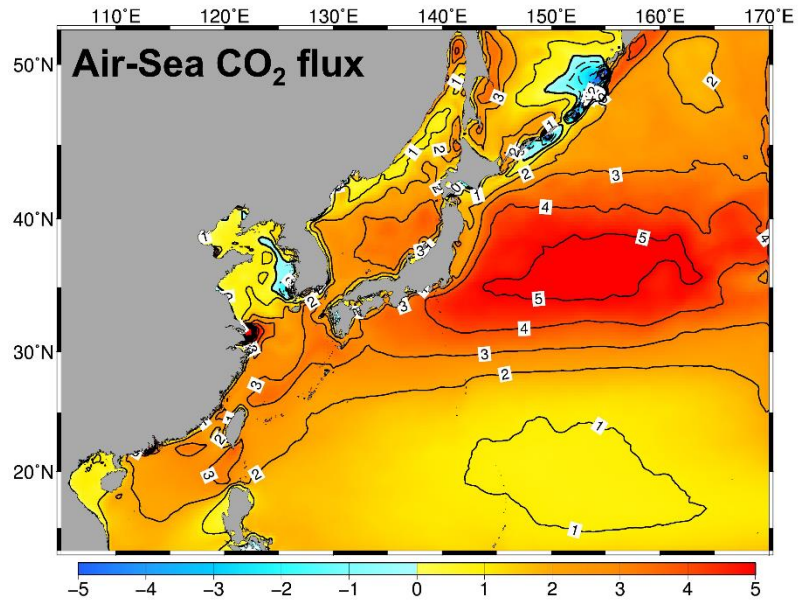
Fig. 16. Distribution of the annual mean air–sea CO_2 flux (mol m^{-2} day^{-1}) in NPRT in the
Northwest Pacific. Positive value indicates the absorption from the atmosphere to the ocean.

975

976
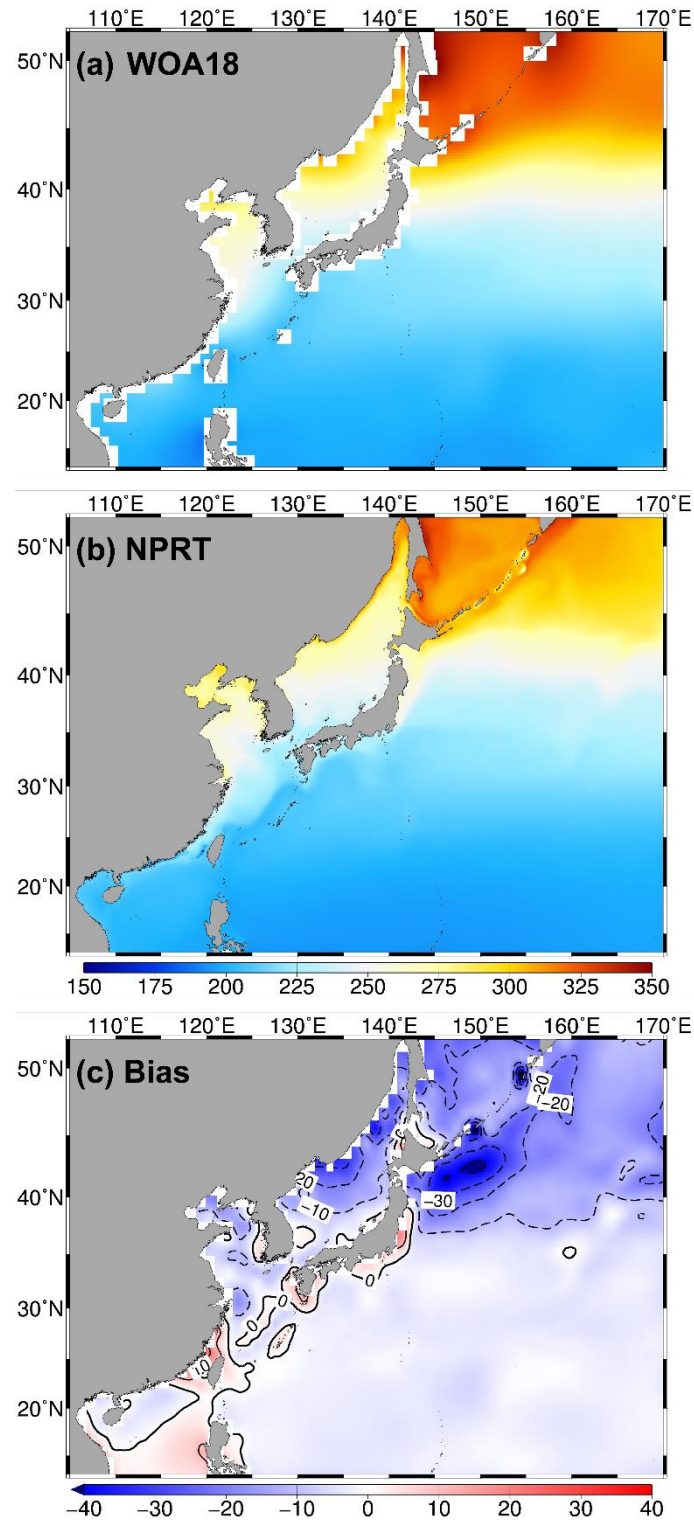
977 **Fig. 17.** Horizontal distributions of the annual mean surface dissolved oxygen (DO)

978 concentration (μmol kg^{-1}) in (a) WOA18 and (b) NPRT, and (c) bias between NPRT and

979 WOA18.

980
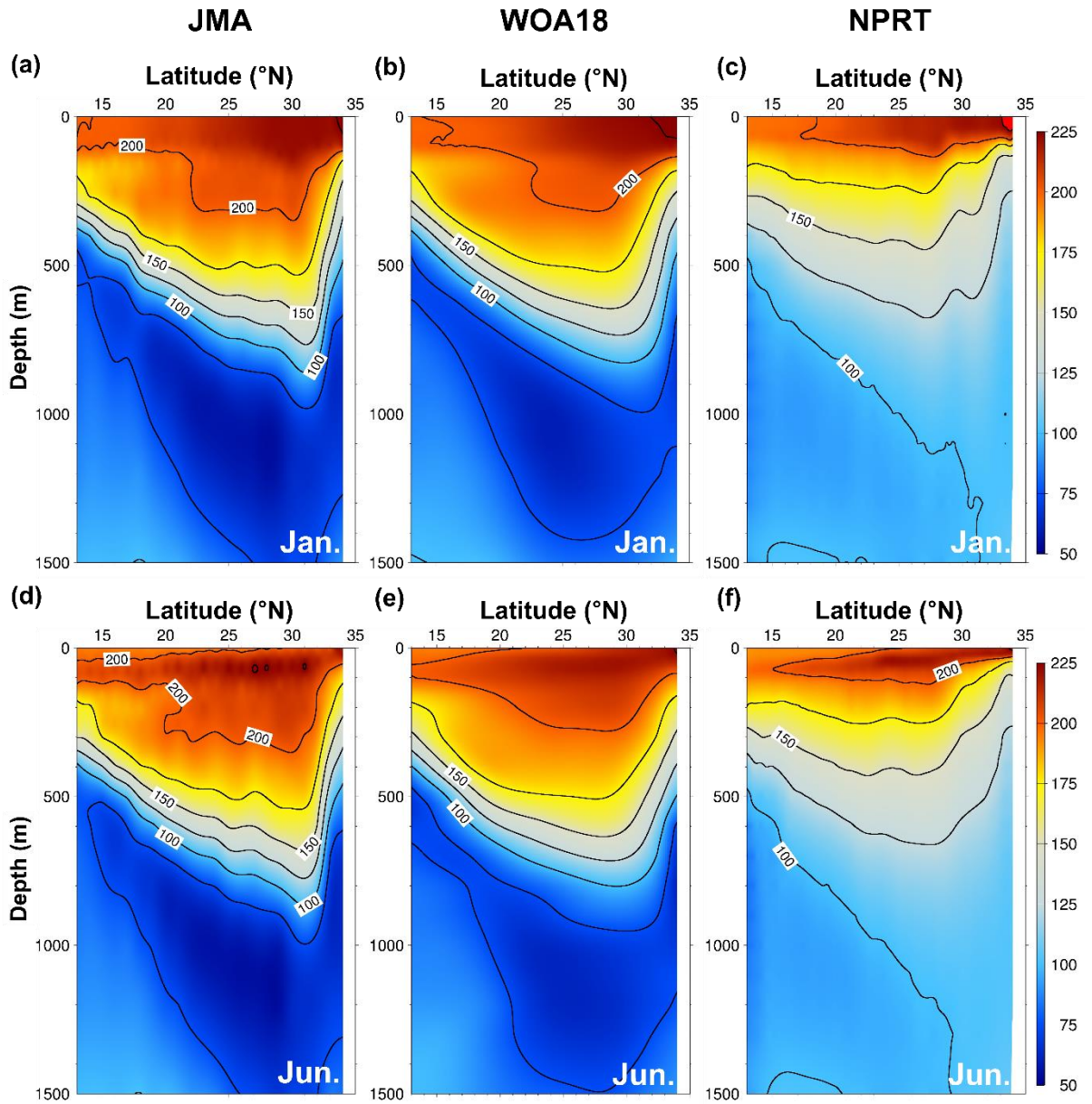
981 **Fig. 18.** Vertical structures of the annual mean dissolved oxygen (DO) concentration (µmol kg⁻

982 ¹) along 137° E line from (a, d) JMA and (b, e) WOA18, and (c, f) NPRT in January (top)

983 and June (bottom).

984

985

986

987 **Table1.** CMIP6 Earth system models were used in this study for comparison with chlorophyll concentration.

Month	Subtropical Region			Subarctic Region			East Sea			YECS		
	NO_3	PO_4	Silicate	NO_3	PO_4	Silicate	NO_3	PO_4	Silicate	NO_3	PO_4	Silicate
1	0.93	1.04	1.77	3.02	2.38	3.44	3.54	3.53	3.32	2.18	1.93	9.54
2	1.36	0.67	2.08	2.77	2.70	3.28	3.70	2.76	5.91	2.93	4.13	13.58
3	1.27	1.22	1.87	2.73	2.82	3.62	2.40	2.29	3.09	2.33	2.53	9.99
4	1.93	1.53	1.74	2.73	2.66	3.86	2.04	1.32	2.59	2.76	1.67	12.77
5	0.79	0.70	1.22	3.44	3.19	3.76	1.83	1.12	2.99	2.93	1.46	5.40
6	1.30	1.68	1.37	3.02	3.58	4.26	2.70	2.63	3.23	3.02	1.80	10.36
7	1.95	2.55	2.10	3.12	3.57	4.23	3.04	2.88	3.44	2.93	2.23	8.58
8	2.49	2.95	2.31	3.27	3.41	4.19	2.97	2.38	4.18	2.78	2.73	10.23
9	2.46	2.60	2.53	2.91	3.41	3.88	2.94	3.29	4.71	2.29	2.26	14.29
10	1.33	1.66	2.15	2.81	3.02	3.57	2.46	2.07	3.99	2.73	2.16	14.36
11	3.97	1.10	1.70	2.61	2.67	4.00	2.03	1.80	3.34	2.09	2.95	13.29
12	4.64	1.86	0.94	2.21	2.47	3.38	3.28	4.42	3.32	2.79	3.76	11.21
13	1.30	0.79	1.40	3.07	3.17	4.19	2.67	2.56	3.68	2.12	2.16	12.61

988

989 **Table2.** CMIP6 Earth system models were used in this study for comparison with chlorophyll concentration.

Model#	Model name	Model center	Physical/Biochemistry model	Data description
1	ACCESS-ESM1-5	CSIRO	MOM5 / WOMBAT	
2	CanESM5	CCCma	NEMO3.4.1 / CMOC	
3	CESM2	NCAR	POP2 / MARBL	
4	CESM2-WACCM	NCAR	POP2 / MARBL	depth-averaged
5	CESM2-WACCM-FV2	NCAR	POP2 / MARBL	data
6	CMCC-ESM2	CMCC	NEMO3.6 / BFM5.2	
7	MPI-ESM1-2-HR	MPI-M	MPIOM1.63 / HAMOCC6	
8	MPI-ESM1-2-LR	MPI-M	MPIOM1.63 / HAMOCC6	
9	CanESM5-1	CCCma	NEMO3.4.1 / CMOC	
10	EC-Earth3-CC	EC-Earth-Consortium	NEMO3.6 / PISCES v2	Surface
11	MPI-ESM-1-2-HAM	HAMMOZ-Consortium	MPIOM1.63 / HAMOCC6	data
12	NorESM2-LM	NCC	MICOM / HAMOCC	
13	NorESM2-MM	NCC	MICOM / HAMOCC	

990

Table 3. Summary of the Taylor diagram scores for annual mean surface chlorophyll concentrations in the subtropical and subarctic regions, East Sea, and the Yellow and East China Sea (YECS) in NPRT, each ensemble model in CMIP6, GFDL–ESM2M and GFDL–ESM2G. The subarctic (subtropical) region is north (south) of 40° N in the NWP.

Model	Subtropical Region	Subarctic Region	East Sea	YECS
NPRT	1.21	1.64	1.88	2.32
ACCESS-ESM1-5	2.44	3.36	3.07	2.78
CanESM5	2.48	2.71	3.33	2.72
CESM2	1.77	2.47	2.98	2.62
CESM2-WACCM	1.90	2.70	2.96	2.65
CESM2-WACCM-FV2	1.74	2.56	2.92	2.66
CMCC-ESM2	2.72	2.84	3.29	2.79
MPI-ESM1-2-HR	4.32	2.20	3.01	2.58
MPI-ESM1-2-LR	5.77	3.19	2.98	2.73
CanESM5-1	2.13	3.42	3.09	3.50
EC-Earth3-CC	1.60	2.27	2.76	2.27
MPI-ESM-1-2-HAM	2.33	3.29	3.02	3.78
NorESM2-LM	2.22	2.21	2.82	2.60
NorESM2-MM	2.39	2.39	2.81	2.68
GFDL-ESM2M	2.96	4.80	3.06	3.06
GFDL-ESM2G	3.02	3.53	2.73	3.43

995